### nature materials

**Article** 

https://doi.org/10.1038/s41563-023-01694-y

# Electrical switching of the edge current chirality in quantum anomalous Hall insulators

Received: 2 January 2023

Accepted: 18 September 2023

Published online: 19 October 2023



Check for updates

Wei Yuan  $\mathbb{O}^{1,3}$ , Ling-Jie Zhou  $\mathbb{O}^{1,3}$ , Kaijie Yang  $\mathbb{O}^{1,3}$ , Yi-Fan Zhao  $\mathbb{O}^{1,3}$ , Ruoxi Zhang  $\mathbb{O}^{1,3}$ , Zijie Yan 1, Deyi Zhuo, Ruobing Mei, Yang Wang, Hemian Yi, Moses H. W. Chan<sup>1</sup>, Morteza Kayyalha **©**<sup>2</sup>, Chao-Xing Liu **©**<sup>1</sup> ⋈ & Cui-Zu Chang <sup>1</sup>□

A quantum anomalous Hall (QAH) insulator is a topological phase in which the interior is insulating but electrical current flows along the edges of the sample in either a clockwise or counterclockwise direction, as dictated by the spontaneous magnetization orientation. Such a chiral edge current eliminates any backscattering, giving rise to quantized Hall resistance and zero longitudinal resistance. Here we fabricate mesoscopic QAH sandwich Hall bar devices and succeed in switching the edge current chirality through thermally assisted spin-orbit torque (SOT). The well-quantized QAH states before and after SOT switching with opposite edge current chiralities are demonstrated through four- and three-terminal measurements. We show that the SOT responsible for magnetization switching can be generated by both surface and bulk carriers. Our results further our understanding of the interplay between magnetism and topological states and usher in an easy and instantaneous method to manipulate the QAH state.

The success of next-generation electronic and spintronic devices hinges on the creation of a reliable material platform with robust and low-energy-consumption quantum states that are feasible for manipulations and measurements. The topological states of matter are appealing due to their intrinsic protection against impurity scattering<sup>1,2</sup>. The quantum anomalous Hall (QAH) state is one example of such topological states<sup>3-9</sup>. It possesses quantized Hall resistance with a dissipationless chiral edge current (CEC), similar to the integer quantum Hall effect<sup>10</sup> but without the need for an external magnetic field. The QAH effect was first discovered in magnetically doped topological insulators (TIs), specifically, Cr- and V-doped (Bi,Sb), Te<sub>3</sub> thin films<sup>8,9</sup>. The resistance-free QAH CEC has been predicted to have potential applications in next-generation energy-efficient electronics and spintronics as well as quantum information applications3.

In QAH insulators, the edge states are spin-polarized and their chiralities are determined by internal magnetization, which leads to a unique locking between the magnetization direction and the propagating direction of the CEC (that is, the chirality) (Fig. 1a,b). The Hall resistance can be used as a probe to identify both the magnetization direction and the edge current chirality. So far, the edge current chirality (that is, right- or left-handed propagating directions) can be changed only by sweeping the external magnetic field  $\mu_0 H$  back and forth<sup>3,8,9,11–15</sup>. However, this would be a cumbersome procedure in real CEC-based electronic devices. The ability to switch the edge current chirality  $instantaneously\,without\,sweeping\,the\,external\,magnetic\,field\,is\,essendant and all the standard control of the standard contr$ tial for the development of CEC-based computation and information technologies. In QAH insulators, the locking between the magnetism and the edge current chirality creates an opportunity to electrically switch the chirality of the edge current by reversing the magnetization direction through spin-orbit torque (SOT)<sup>16,17</sup>. Current-driven SOT has been proved to be an efficient mechanism for magnetization switching in bulk insulating TI-based films/heterostructures, including Cr-doped

Department of Physics, The Pennsylvania State University, University Park, PA, USA. Department of Electrical Engineering, The Pennsylvania State University, University Park, PA, USA. 3These authors contributed equally: Wei Yuan, Ling-Jie Zhou, Kaijie Yang. 🖂 e-mail: cxl56@psu.edu; cxc955@psu.edu

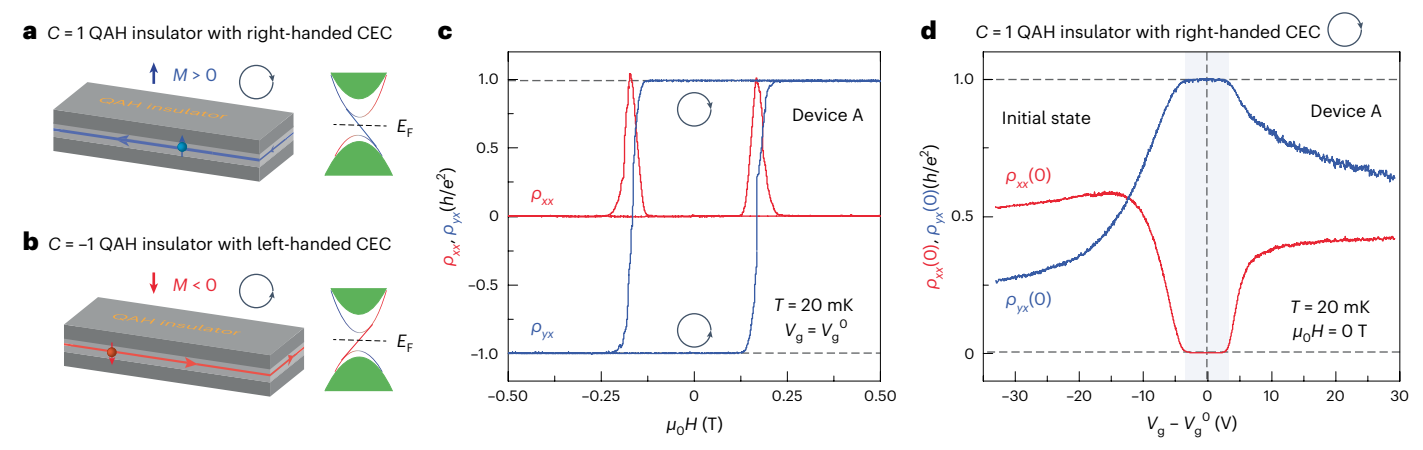


**Fig. 1**| **Edge current chirality in QAH insulators. a,b**, Schematics of QAH insulator sandwiches with right-handed (a) and left-handed (b) CEC. The CEC is shown in real (left) and momentum space (right) for positive (a) and negative (b) magnetization. *C*, Chern number. **c**, Dependence of  $\rho_{xx}$  (red) and  $\rho_{yx}$  (blue) on  $\mu_0 H$  measured at  $V_g = V_g^0 = +0.8$  V and T = 20 mK.  $\rho_{yx}(0) \approx +h/e^2$  and  $\rho_{yx}(0) \approx -h/e^2$ 

correspond to right- and left-handed CEC, respectively.  $V_{\rm g}$ , bottom gate voltage;  $V_{\rm g}^{\,\,0}$ , charge-neutral point of the QAH insulator; h, Planck's constant; e, elementary charge.  ${\bf d}$ , Dependence of  $\rho_{\rm yx}(0)$  (blue) and  $\rho_{\rm xx}(0)$  (red) on  $V_{\rm g}-V_{\rm g}^{\,\,0}$  for the C=1 QAH insulator with right-handed CEC at  $\mu_0H=0$  T and T=20 mK.

(Bi,Sb)<sub>2</sub>Te<sub>3</sub> films<sup>18</sup> as well as (Bi,Sb)<sub>2</sub>Te<sub>3</sub>/ferromagnet<sup>19-21</sup> and Cr-doped (Bi,Sb)<sub>2</sub>Te<sub>3</sub>/(Bi,Sb)<sub>2</sub>Te<sub>3</sub> bilayers<sup>22,23</sup>. The SOT effect in these bulk insulating TI-based films/heterostructures is a result of the charge-to-spin conversion induced by the Rashba-Edelstein effect of helical surface states [also called the inverse spin-galvanic effect (ISGE)]16,17,24. However, SOT switching has not been demonstrated in any magnetic TI films/heterostructures that host the QAH state with dissipationless CEC. To realize electrical SOT switching in QAH insulators, the sample needs to satisfy two conditions: (1) the QAH structure must provide a large SOT effect; and (2) the current density must be high enough for magnetization switching. Condition (1) can be achieved in QAH films in which an asymmetric potential between the top and bottom surfaces is induced by their different environments. Condition (2) can be achieved by fabricating micrometre-sized mesoscopic QAH sandwich Hall bar devices<sup>25</sup>, which increases the current density. Since the top and bottom magnetic TI layers in QAH sandwiches have similar magnetic moments, these two magnetically doped TI layers switch their magnetization simultaneously. After SOT magnetization switching, the OAH insulator with opposite edge current chirality is induced.

In this work, we fabricate QAH sandwich Hall bar devices that have a width of ~1–10 um using electron-beam lithography (Methods)<sup>25</sup>. By performing four- and three-terminal transport measurements<sup>26</sup>, we demonstrate the electrical switching of the QAH edge current chirality through thermally assisted SOT. We find that the C = 1 QAH insulator with a right-handed CEC can be switched to the C = -1 QAH insulator with a left-handed CEC by applying a current pulse under an in-plane magnetic field. Since the SOT magnetization switching ratio is easily greater than the quantum percolation threshold of magnetic domains<sup>27,28</sup>, a well-quantized QAH state with the opposite edge current chirality usually appears after the magnetization switching. This unique property makes the electrical switching of the edge current chirality robust and reliable in real QAH electronic devices. We show that SOT in QAH insulators can be induced by the ISGE from both surface and bulk carriers. Our calculations show a strong contribution of SOT from the hole bands of surface states, which share the same sign as that from the first bulk valence quantum-well (QW) sub-bands, consistent with experimental observations.

The QAH insulators used in this work comprise the 3QL Cr-doped  $(Bi,Sb)_2Te_3/4QL$   $(Bi,Sb)_2Te_3/3QL$  Cr-doped  $(Bi,Sb)_2Te_3$  sandwich structure (where QL denotes a quintuple layer), referred to as a 3-4-3 QAH sandwich. These sandwich structures are grown on heat-treated insulating SrTiO<sub>3</sub>(111) substrates in a molecular beam epitaxy (MBE)

chamber with a vacuum better than  $2 \times 10^{-10}$  mbar. The SrTiO<sub>3</sub>(111) substrate is also used as the dielectric in regulating the bottom gate voltage  $V_{\rm g}$  to tune the chemical potential  $E_{\rm F}$  of the QAH samples. The electrical-transport measurements are carried out using a physical property measurement system (PPMS) with a horizontal rotator and in a dilution refrigerator (10 mK) cryostat with a vector magnet (9-1-1 T). Six-terminal Hall bars with bottom gate electrodes are used for electrical-transport studies. More details about the MBE growth, device fabrication and electrical-transport measurements can be found in the Methods.

### Characterization of the QAH edge current chirality

We first confirm the QAH state in a 3-4-3 sandwich Hall bar device with a width  $w \approx 5 \,\mu\text{m}$  (Device A; Extended Data Fig. 1) by performing electrical-transport measurements at the temperature T = 20 mK. Figure 1c shows the  $\mu_0 H$  dependence of the Hall resistance  $\rho_{vx}$  and the longitudinal resistance  $\rho_{xx}$  at the charge-neutral point  $V_g = V_g^0 = +0.8 \text{ V}$ . For positive magnetization M > 0,  $\rho_{yx}$  has a quantized value of around  $+0.9919 \pm 0.0023 \, h/e^2$  and  $\rho_{xx} \approx 0.0029 \pm 0.0007 \, h/e^2$  (~74 ± 18  $\Omega$ ) under zero magnetic field, corresponding to the C = 1 QAH state with right-handed CEC (Fig. 1a). Using an external magnetic field to switch the magnetization polarity (that is, for negative magnetization M < 0),  $\rho_{vx}$  displays a negative quantized value of around  $-0.9954 \pm 0.0019 \ h/e^2$ and  $\rho_{xx} \approx 7 \times 10^{-5} \pm 0.0002 \, h/e^2 \, (-2 \pm 5 \, \Omega)$  under zero magnetic field, giving rise to the C = -1 QAH state with left-handed CEC (Fig. 1b). The well-quantized QAH state is confirmed by the  $V_{\sigma}$  dependence of  $\rho_{vx}$  and  $\rho_{xx}$  at zero magnetic field  $[\rho_{yx}(0)]$  and  $\rho_{xx}(0)$ , respectively (Fig. 1d). We set the initial state at M > 0, and  $\rho_{vx}(0)$  exhibits a distinct plateau at a positive quantized value of ~0.9978  $\pm$  0.0027  $h/e^2$ , concomitant with  $\rho_{xx}(0) \approx 0.0028 \pm 0.0006 \, h/e^2$ , centred at  $V_g = V_g^0$  (Fig. 1d). Therefore, the sample is initially in the C = 1 QAH state with right-handed CEC (Fig. 1a). We will next investigate if the QAH edge current chirality can be electrically switched via the SOT effect by applying a current pulse.

#### The SOT effect in a QAH sandwich

In a magnetic TI sandwich near the bulk insulating regime, an electrical current  $J_e$  along the x axis can generate spin accumulation  $S_y$  along the y axis at the magnetic TI/TI interface and exerts a damping-like torque  $\tau_{SO} \propto \mathbf{M} \times (\mathbf{M} \times S_y \hat{y}) = -\mathbf{M} \times \mu_0 H_{SO}$  (refs. 18–20,22,23) (Fig. 2a) on the magnetic moment  $\mathbf{M}$ , where  $\hat{y}$  is the unit vector along the y axis and  $\mu_0 H_{SO} \propto S_y \hat{y} \times \mathbf{M}$  is known as an effective spin–orbit field. Therefore,

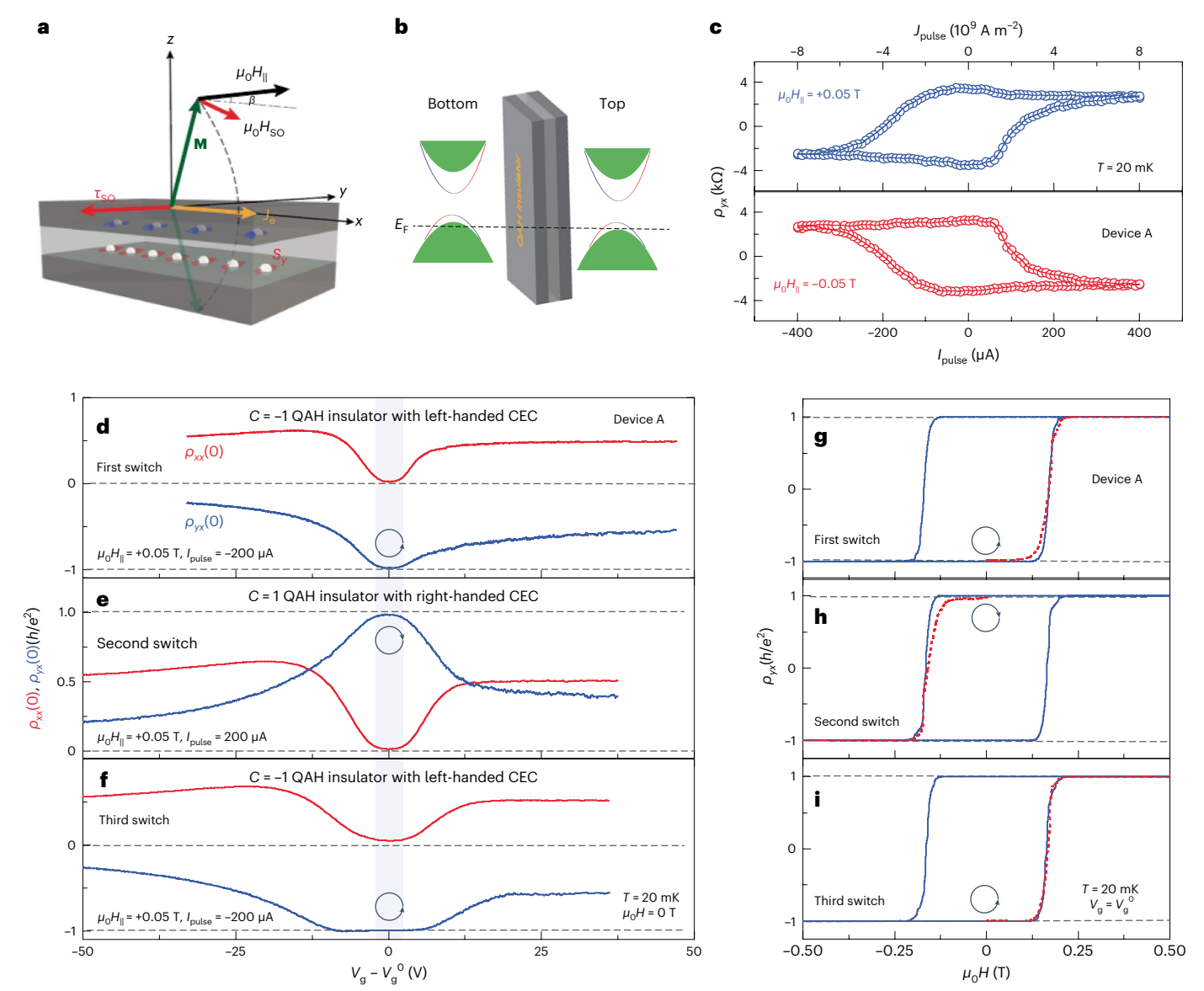


**Fig. 2** | **Electrical switching of the QAH CEC through bulk and surface carriers. a**, Schematic of the SOT magnetization switching in a QAH sandwich under an in-plane external magnetic field. The angle between the x axis and the direction of the in-plane external magnetic field  $|\beta|$  is less than  $4^{\circ}$ . **b**, Schematic of the magnetic TI sandwich with symmetry-inequivalent top and bottom surfaces. **c**, Dependence of  $\rho_{yx}$  on the current pulse  $I_{pulse}$  under an in-plane magnetic field  $\mu_0 H_{\parallel} = \pm 0.05$  T at T = 20 mK. The corresponding current pulse density  $J_{pulse}$  is shown on the upper horizontal axis. The SOT switching is carried out at

 $\rho_{yx}(0) \approx +0.27 \, h/e^2$ . **d-f**, Dependence of  $\rho_{yx}(0)$  (blue) and  $\rho_{xx}(0)$  (red) on  $V_g - V_g^0$  after the first switch with  $I_{\text{pulse}} \approx -200 \, \mu\text{A}$  (**d**), the second switch with  $I_{\text{pulse}} \approx 200 \, \mu\text{A}$  (**e**) and the third switch with  $I_{\text{pulse}} \approx -200 \, \mu\text{A}$  (**f**) under  $\mu_0 H_{\parallel} = +0.05 \, \text{T}$ . The data shown are measured at zero magnetic field. **g-i**, Dependence of  $\rho_{yx}$  on  $\mu_0 H$  at  $V_g = V_g^0$  and  $T = 20 \, \text{mK}$  after the first (**g**), second (**h**) and third (**i**) switches. The red dashed curves correspond to the initial magnetization process after each switching.

when a small in-plane magnetic field  $\mu_0 H_\parallel$  is applied parallel (antiparallel) to the electrical current direction,  $\mu_0 H_{SO}$  drives  ${\bf M}$  along the positive (negative) direction in a QAH sandwich (Fig. 2a). Since the carriers on its two magnetic TI/TI interfaces have opposite spin polarization,  $\tau_{SO}$  from two symmetry-equivalent surfaces of the QAH sandwich cancels each other (Fig. 2a). Therefore, to induce SOT in QAH insulators, we need an asymmetric potential between two surfaces (Fig. 2b).

The application of a single bottom gate voltage  $V_{\rm g}$  inevitably induces an asymmetric potential in a QAH sandwich<sup>29</sup>. Moreover, the introduction of some dissipative bulk conducting channels may also enhance the SOT effect through the spin Hall effect<sup>17</sup>. Therefore, we first tune  $V_{\rm g}$  to make  $\rho_{\rm jx}(0) \approx +0.27 \ h/e^2$  (around +7.00 k $\Omega$ ) when the chemical potential (as denoted by the black dashed line) crosses both bulk valence bands and surface states (Fig. 2b). By injecting a series

of current pulses with a duration  $\Delta t \approx 5$  ms, we examine the SOT magnetization switching at  $\rho_{yx}(0) \approx +0.27 \ h/e^2$  under  $\mu_0 H_\parallel = \pm 0.05$  T. After SOT switching, the maximum value of  $\rho_{yx}(0)$  is only ~0.14  $h/e^2$  (~3.6 k $\Omega$ ) because the magnetization moment is not fully switched (Fig. 2c). We choose  $\mu_0 H_\parallel = \pm 0.05$  T because it is much smaller than the anisotropy field  $K \approx 0.7$  T of our QAH sandwiches (Extended Data Figs. 2 and 3). The values of  $\rho_{yx}$  shown in Fig. 2c are measured at an excitation current of ~1 nA after injecting each current pulse. We note that the current pulse duration  $\Delta t \approx 5$  ms is much longer than the incubation period of the SOT process in the nanosecond timescale 17,30. Therefore, the SOT effect in our experiments is thermally assisted (Supplementary Section 3). We find that the switching polarity is determined by the current pulse and the in-plane magnetic field directions, consistent with the SOT geometry (Fig. 2a). The current pulse  $|I_{pulse}| \approx 200 \ \mu \text{A}$  is sufficient for the

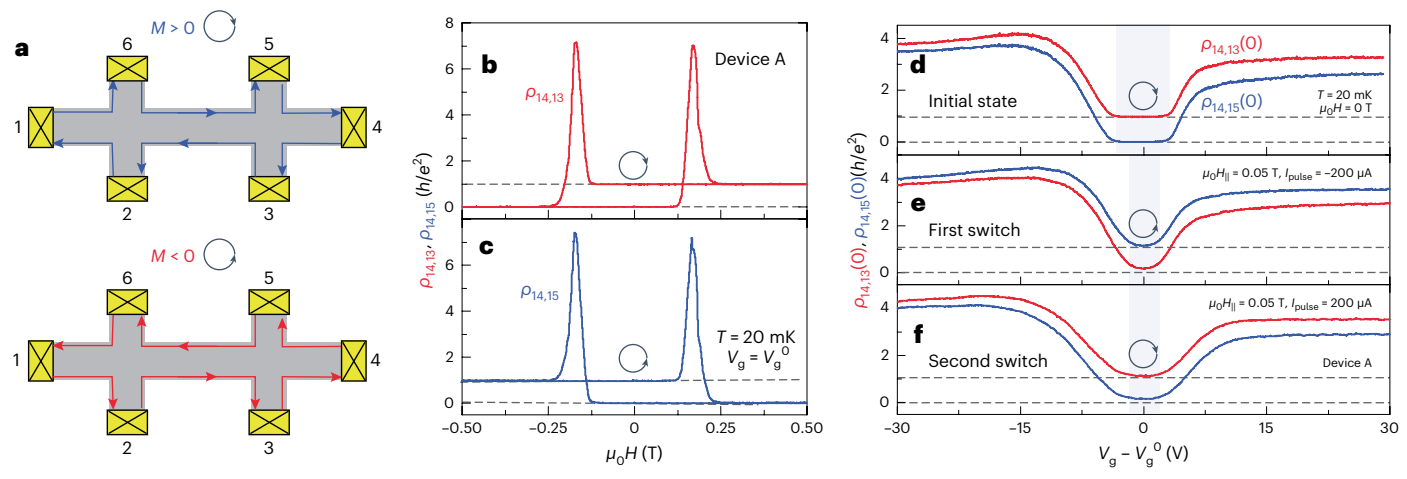


**Fig. 3** | **QAH CEC switching through three-terminal measurements. a**, Schematics of chiral edge channels when the current flows from 1 to 4. The blue and red lines indicate right- and left-handed CEC for positive and negative magnetization, respectively. **b,c**, Dependence of the three-terminal resistances

 $\rho_{14,13}(\mathbf{b})$  and  $\rho_{14,15}(\mathbf{c})$  on  $\mu_0 H$  at  $V_g = V_g^0$  and T = 20 mK.  $\mathbf{d} - \mathbf{f}$ , Dependence of  $\rho_{14,15}(0)$  (red) and  $\rho_{14,15}(0)$  (blue) on  $V_g - V_g^0$  at the initial state ( $\mathbf{d}$ ), after the first switch with  $I_{\text{pulse}} \approx -200 \, \mu\text{A}$  ( $\mathbf{e}$ ) and after the second switch with  $I_{\text{pulse}} \approx 200 \, \mu\text{A}$  ( $\mathbf{f}$ ) under  $\mu_0 H_0 = +0.05$  T. The data shown are measured at zero magnetic field.

SOT magnetization switching in Device A ( $w=5~\mu m$ ). The corresponding current pulse density  $J_{\rm pulse}$  is shown on the upper horizontal axis of Fig. 2c. The critical current density for SOT magnetization switching is found to be ~4 × 10<sup>9</sup> A m<sup>-2</sup>, which is around the same order of magnitude as that in bulk insulating TI-based films/heterostructures <sup>18–20,22,23</sup> but a few orders of magnitude smaller than that in heavy metal/ferromagnet heterostructures <sup>17,31,32</sup>.

## Electrical switching of the QAH CEC through both bulk and surface carriers

Next, we use the SOT effect induced by both bulk and surface carriers in magnetic TI sandwiches to realize the electrical switching of the edge current chirality. We start with the C = 1 QAH state with right-handed CEC as the initial state (Fig. 1a,d) and carry out four switchings of the edge current chirality in Device A ( $w = 5 \mu m$ ) by changing the direction of either  $\mu_0 H_{\parallel}$  or  $I_{\text{pulse}}$  (Figs. 2 and 3, Extended Data Fig. 4 and Supplementary Table 1). Before each switching, we tune  $V_g$  so that  $|\rho_{vx}(0)| \approx 0.27 \ h/e^2$ , where the SOT effect can be considered to be induced by both bulk valence bands and surface states. For the first switching, we apply a current pulse  $I_{\text{pulse}} \approx -200 \,\mu\text{A} \,\text{under} \,\mu_0 H_{\parallel} = +0.05 \,\text{T}$ , and  $\rho_{yx}(0)$  is switched from around  $+0.2789 h/e^2$  to approximately  $-0.2321 h/e^2$ , indicating that the majority of magnetization is switched from a positive to a negative direction (Fig. 2d). Under zero magnetic field, we use  $V_g$  to tune the chemical potential back to the magnetic exchange gap and find that  $\rho_{yy}(0)$  displays a plateau with a negative quantized value of around  $-0.9836 \pm 0.0019 \ h/e^2$ , concomitant with  $\rho_{xx}(0) \approx 0.0229 \pm 0.0006 \ h/e^2$ at  $V_g = V_g^0$  (Fig. 2d). After the first switching, the sample behaves as a C = -1 QAH insulator with left-handed CEC (Fig. 1b), which is validated by measuring the initial magnetization curves at  $V_g = V_g^0$  (Fig. 2g). For the second, third and fourth switchings, by changing the direction of either  $\mu_0 H_{\parallel}$  or  $I_{\text{pulse}}$ , we find that  $\rho_{yx}(0) \approx +0.9833 \pm 0.0018 \ h/e^2$ and  $\rho_{xx}(0) \approx 0.0163 \pm 0.0003 \, h/e^2$  after the second switching,  $\rho_{vx}(0) \approx -0.9953 \pm 0.0007 \ h/e^2 \ \text{and} \ \rho_{xx}(0) \approx 0.0476 \pm 0.0006 \ h/e^2$ after the third switching, and  $\rho_{vx}(0) \approx +0.9862 \pm 0.0009 \ h/e^2$  and  $\rho_{xx}(0) \approx 0.0219 \pm 0.0007 \ h/e^2$  after the fourth switching at  $V_g = V_g^0$ (Fig. 2e, f and Extended Data Fig. 4a, respectively). These observations confirm that the sample behaves as a QAH insulator with right-, leftand right-handed CEC after the second, third and fourth switchings, respectively. The current edge chiralities are confirmed by measuring the initial magnetization curves at  $V_g = V_g^0$  (Fig. 2h,i and Extended Data Fig. 4b, respectively). For Device A, the SOT magnetization switching ratio at  $|\rho_{vx}(0)| \approx 0.27 \ h/e^2$  by applying  $|I_{\text{pulse}}| \approx 200 \ \mu\text{A}$  under

 $\mu_0 H_{\parallel}$  = +0.05 T is estimated to be ~83.9% (Extended Data Fig. 3), but the well-quantized QAH insulator emerges by tuning the gates after each switching. This behaviour is a result of the quantum percolation property in QAH insulators<sup>27,28</sup>. We note that the  $V_{\rm g}^{\,0}$  values after each switching are not identical, presumably due to the hysteretic ferroelectric property of the SrTiO<sub>3</sub> substrate<sup>3,33</sup> (Supplementary Section 10).

To demonstrate further the electrical switching of the edge current chirality in QAH insulators, we perform three-terminal measurements on Device A after each switching (Fig. 3a). Figure 3b,c shows the dependence of the three-terminal resistances  $\rho_{14,13}$  and  $\rho_{14,15}$  on  $\mu_0 H$  at T = 20 mK and  $V_g = V_g^0$ . At zero magnetic field,  $\rho_{14,13} \approx h/e^2$  and  $\rho_{14,15} \approx 0$ for M > 0, corresponding to a C = 1QAH insulator with right-handed CEC (Fig. 1a). For M < 0,  $\rho_{14.13} \approx 0$  and  $\rho_{14.15} \approx h/e^2$ , corresponding to a C = -1QAH insulator with left-handed CEC (Fig. 1b). Figure 3d-f shows the dependence of  $\rho_{14,13}$  and  $\rho_{14,15}$  under zero magnetic field [ $\rho_{14,13}(0)$  and  $ho_{14,15}(0)$ , respectively] on  $V_{\rm g}$  –  $V_{\rm g}^{\ 0}$  at the initial QAH state and for the QAH states after the first and second switches. At  $V_g = V_g^0$ ,  $\rho_{14.13}(0) \approx h/e^2$ and  $\rho_{14.15}(0) \approx 0$  validate that both the initial state and the state after the second switch are the C = 1 QAH insulator with right-handed CEC, and  $\rho_{14,13}(0) \approx 0$  and  $\rho_{14,15}(0) \approx h/e^2$  validate that the state after the first switch is the C = -1 QAH insulator with left-handed CEC. Therefore, we establish that the QAH edge current chirality can be reproducibly switched by the injection of current pulses under an in-plane magnetic field through the SOT effect induced by both bulk and surface carriers (Extended Data Figs. 4 and 5).

### Electrical switching of the QAH CEC through surface carriers

In addition to SOT generated by both bulk and surface carriers, we use the SOT effect induced by only surface carriers to switch the edge current chirality. We apply a current pulse on magnetic TI sandwiches at  $V_g = V_g^0$  under an in-plane magnetic field (Fig. 4a) and investigate whether or not the C=1 QAH insulator can be switched to the C=-1 QAH insulator (Fig. 4b). For Device A,  $\rho_{yx}(0) \approx +1.0005 \pm 0.0020 \, h/e^2$  and  $\rho_{xx}(0) \approx 0.0220 \pm 0.0007 \, h/e^2$  at  $V_g = V_g^0$ , corresponding to the right-handed CEC. By applying  $I_{\text{pulse}} \approx -200 \, \mu\text{A}$  under  $\mu_0 H_{\parallel} = +0.05 \, \text{T}$  at  $V_g = V_g^0$ ,  $\rho_{yx}(0)$  is found to be around  $-0.4552 h/e^2$  and  $\rho_{xx}(0)$  is  $-0.6166 h/e^2$ , suggesting that the device is tuned away from the QAH regime. After the current pulse, we vary  $V_g$  to tune the sample back into the QAH state with  $\rho_{yx}(0) \approx -1.0008 \pm 0.0011 \, h/e^2$  and  $\rho_{xx}(0) \approx 0.0564 \pm 0.0006 \, h/e^2$  at  $V_g = V_g^0$ , corresponding to the left-handed CEC (Fig. 4c). We replicate this phenomenon in a QAH

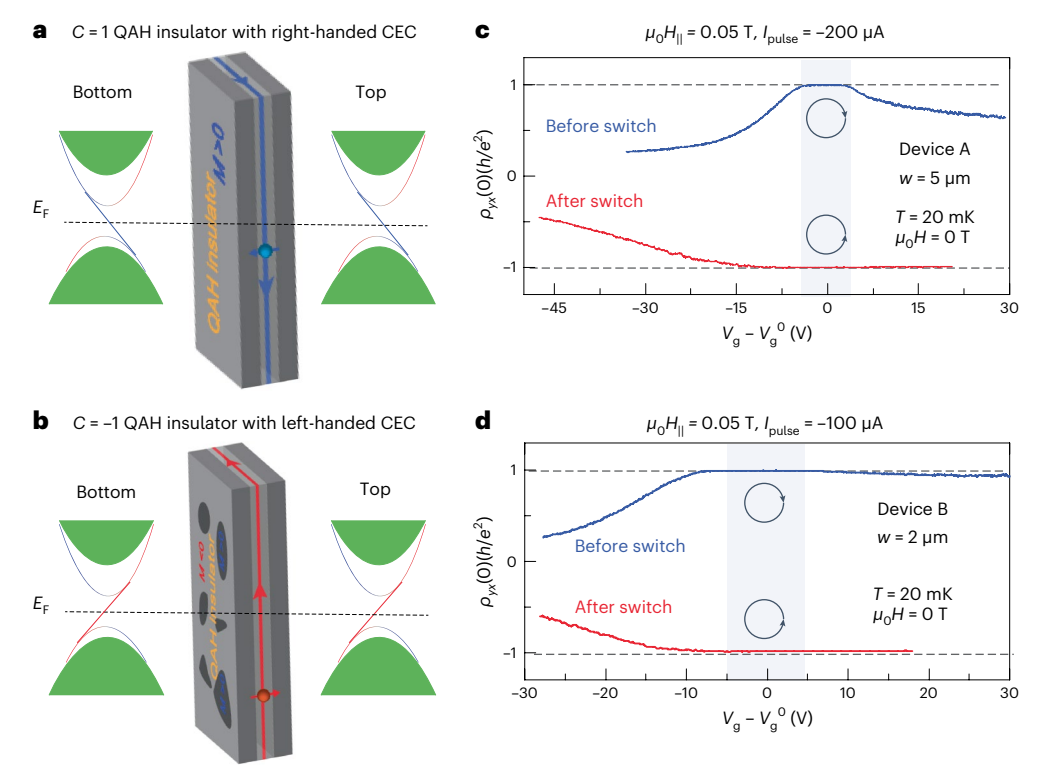


**Fig. 4** | **Electrical switching of the QAH CEC through surface carriers. a**, Schematic of the initial C=1 QAH sandwich with fully aligned positive magnetization. **b**, Schematic of the C=-1 QAH sandwich heterostructure with percolating negative magnetization after SOT switching at  $V_{\rm g}=V_{\rm g}^{~0}$ . The dark grey areas depict the magnetic domains that fail to switch. Owing to the quantum percolation property, the sample still shows a well-quantized C=-1 QAH effect. **c**, Dependence of  $\rho_{\rm yx}(0)$  on  $V_{\rm g}-V_{\rm g}^{~0}$  for Device A (w=5 µm) before (blue) and after

(red) magnetization switching at  $V_{\rm g}=V_{\rm g}^{\rm \, 0}$  with  $I_{\rm pulse}\approx-200$   $\mu{\rm A}$  under  $\mu_0H_{\parallel}=+0.05$  T at T=20 mK. The  $V_{\rm g}^{\rm \, 0}$  values are +49.5 V and +54.0 V before and after SOT magnetization switching, respectively.  ${\bf d}$ , Dependence of  $\rho_{\rm px}(0)$  on  $V_{\rm g}-V_{\rm g}^{\rm \, 0}$  for Device B (w=2  $\mu{\rm m}$ ) before (blue) and after (red) magnetization switching at  $V_{\rm g}=V_{\rm g}^{\rm \, 0}$  with  $I_{\rm pulse}\approx-100$   $\mu{\rm A}$  under  $\mu_0H=+0.05$  T at T=20 mK. The  $V_{\rm g}^{\rm \, 0}$  values are +50.0 V and +52.0 V before and after SOT magnetization switching, respectively.

sandwich Hall bar device of width  $w \approx 2 \, \mu m$  (Device B; Extended Data Figs. 6–8). In Device B, we use  $I_{\text{pulse}} \approx -100 \, \mu \text{A}$  due to its narrower width (Extended Data Fig. 9). Here,  $\rho_{yx}(0) \approx +0.9999 \pm 0.0007 \, h/e^2$  and around  $-0.6005 h/e^2$  before and after the switching process, respectively. By tuning  $V_g$ ,  $\rho_{yx}(0) \approx -0.9865 \pm 0.0009 \, h/e^2$  at  $V_g = V_g^0$ , concomitant with  $\rho_{xx}(0) \approx 0.0072 \pm 0.0002 \, h/e^2$ , verifying the left-handed CEC after switching (Fig. 4d). Therefore, we show that the edge current chirality can be switched through surface carrier-induced SOT when the magnetic TI sandwich is near the QAH regime.

We next discuss two possible origins for electrical switching of the edge current chirality at  $V_g = V_g^0$ . First, we find that the sample is usually tuned away from the QAH regime after the injection of the current pulse at  $V_g = V_g^0$ , which in turn induces an asymmetric potential on two surfaces of the QAH samples<sup>29</sup>. After SOT switching,  $\rho_{vx}(0)$  is around  $-0.4552h/e^2$  and  $-0.6005h/e^2$  for Devices A and B, respectively (Fig. 4c,d). Both values indicate that the SOT induced by surface carriers plays a dominant role in magnetization and edge current chirality switching<sup>3</sup>. Second, the current pulse of hundreds of microamperes is much larger than the breakdown current (tens to hundreds of nanoamperes) of the QAH insulators  $^{23,34,35}$ , so the QAH state must have been broken down after injecting the current pulse at  $V_g = V_g^0$ , due to the current-pulse-induced heating effect (Supplementary Section 3). After the breakdown of the QAH state, the surface carriers are excited by the current pulse, creating a finite SOT to induce magnetization switching. Moreover, we note that the quantum percolation property of the QAH insulators greatly facilitates the electrical switching of the edge current chirality (Extended Data Fig. 8). Provided that the SOT magnetization switching ratio through the bulk/surface carrier-generated SOT is greater than the quantum percolation threshold of the magnetic

domains in magnetic TI sandwiches<sup>27,28</sup>, a well-quantized QAH state appears after each switching (Fig. 4b).

#### Spin susceptibility in a QAH sandwich

As noted above, in QAH sandwiches,  $\tau_{SO}$  can be generated by spin polarization S from the ISGE of the surface and/or bulk carriers. The ISGE induces  $S_{ISGE} \approx (\hat{z} \times E)$  (refs. 18,19,23,36) (Fig. 2a), which can be evaluated from the response function  $\chi_{yx}$  that connects spin polarization to an electric field E through  $S_i = \sum_i \chi_{ij} E_j$  with i,j = x,y,z (Methods).

Here  $\hat{z}$  is the unit vector along the z axis. As the QAH insulators are bulk insulating, the major mechanism is expected from the spin polarization of the surface carriers (Supplementary Sections 2, 11 and 12) $^{21,22,37}$ . Magnetic switching can be caused by the damping-like torque from  $S_{\rm ISGE}$  via  $\tau_{\rm SO,ISGE} \propto \mathbf{M} \times (\mathbf{M} \times S_{\rm ISGE})$ . Other possible mechanisms for SOT, including the bulk spin Hall effect (Supplementary Sections 2 and 11) and magnetoelectric coupling from surface Hall currents (refs. 38,39) (Supplementary Sections 12 and 13), are also discussed.

Next, we model the QAH sandwiches of thickness  $L = (L_1 + L_2)$  (Fig. 5a inset) using a four-band Hamiltonian<sup>14,40</sup>

$$\begin{split} H\left(k_{\parallel}, -i\partial_{z}\right) &= \left(D_{0}\left(z\right) - D_{1}\partial_{z}^{2} + D_{2}k_{\parallel}^{2}\right)\sigma_{0}\tau_{z} \\ + A_{0}\left(k_{y}\sigma_{x} - k_{x}\sigma_{y}\right)\tau_{x} - iB_{0}\partial_{z}\sigma_{0}\tau_{y} \\ &+ \left(-C_{1}\partial_{z}^{2} + C_{2}k_{\parallel}^{2}\right)\sigma_{0}\tau_{0} + M(z)\sigma_{z}\tau_{0} + V(z)\sigma_{0}\tau_{0}, \end{split}$$

Here the Pauli matrices  $\tau_{0,x,y,z}$  act on the orbital space and the Pauli matrices  $\sigma_{0,x,y,z}$  act on the spin-1/2 space.  $k_{\parallel}$ ,  $k_x$  and  $k_y$  are the in-plane crystal momenta. The parameters are taken to be  $D_1 = 6.86$  eV Å<sup>2</sup>,  $D_2 = 44.5$  eV Å<sup>2</sup>,

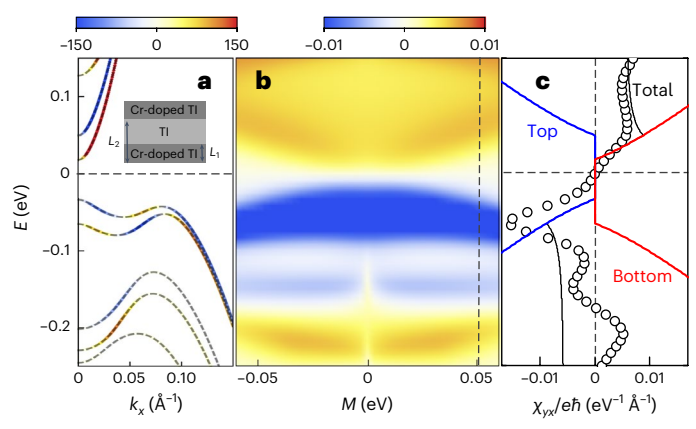


Fig. 5 | Theoretical calculations of  $\chi_{yx}$  in the 3-4-3 QAH sandwich. **a**, Energy spectrum for the 3-4-3 QAH sandwich heterostructure with M=0.05 eV. The colour scale represents the contribution  $\chi_{yx}(k_x,n,E_F=E_{k_xn})$  when the Fermi surface crosses the nth band at  $k_x$ , **b**, Spin response function  $\chi_{yx}$  for the 3-4-3 QAH sandwich heterostructure under different magnetization M and chemical potential  $E_F$ . The colour scale represents the final spin response function  $\chi_{yx}/e\hbar$ , where  $\hbar=h/2\pi$ . **c**, Comparison of  $\chi_{yx}$  from the two-surface-state model (Methods and Supplementary Section 11) and the four-band Hamiltonian of the 3-4-3 QAH sandwich heterostructure. The blue (red) lines are  $\chi_{yx}$  from the top (bottom) surface. The black line is the total of the two surfaces, and the black circles denote points calculated from the 3-4-3 QAH sandwich model with M=0.05 eV, corresponding to the grey vertical dashed line in **b**. Note that the vertical axis in **b** and **c** is the chemical potential  $E_F$ .

 $A_0$  = 3.33 eV Å and  $B_0$  = 2.26 eV Å.  $C_1$  = -6 eV Ų and  $C_2$  = 30 eV Ų are used to tune the relative position of Dirac points and bulk valence bands. M(z) is the magnetization from Cr doping and  $V(z) = V_0 \times (z/L - 1/2)$  is the asymmetric potential along the z direction with  $V_0$  = 0.05 eV. The QAH sandwich with magnetic dopants in the top and bottom surface layers is modelled by

$$D_0(z) = \begin{cases} D_0 & L_1 \le z \le L_2 \\ D_0 + \Delta D_0 & 0 < z < L_1 \text{ or } L_2 < z < L \end{cases}$$

and

$$M(z) = \begin{cases} 0 & L_1 \le z \le L_2 \\ M & 0 < z < L_1 \text{ or } L_2 < z < L \end{cases}$$

with  $D_0 = -0.28$  eV and  $\Delta D_0 = 0.26$  eV. For the 3-4-3 QAH sandwich used in this work,  $L_1 = 3$  nm and  $L_2 = 7$  nm (Fig. 5a inset).

Figure 5a shows the energy spectrum of the 3-4-3 QAH sandwich at a fixed magnetization M = 0.05 eV. The corresponding spin response function  $\chi_{vx}$  as a function of the magnetization M and chemical potential  $E_F$  is shown in Fig. 5b. For  $E_F > -0.1$  eV, the carriers near  $E_F$  come primarily from surface states. A non-zero  $\chi_{vx}$  is found and its sign is reversed from electron-to hole-doped regimes. This sign change can be understood from a two-surface-state model (Fig. 5c; see Methods and Supplementary Section 11). For  $E_F \approx -0.15$  eV, the chemical potential starts to cross the first bulk valence QW sub-bands, and one more peak of  $\chi_{vx}$  with the same sign of the surface-state contribution in the hole-doping regime is seen. A strong hybridization between surface states and bulk QW states is expected in this regime. By further lowering the chemical potential to  $E_F < -0.2$  eV, the second bulk valence QW sub-bands appear and their contribution to  $\chi_{vx}$  has an opposite sign. By comparing our theory and experiments, we conclude that surface states give rise to a strong contribution to the SOT, even larger than the

bulk carrier contribution, which is consistent with our experimental observation of magnetization switching when the chemical potential is tuned near the OAH insulator regime.

To summarize, we fabricated mesoscopic QAH sandwich Hall bar devices and realized electrical switching of the edge current chirality in QAH insulators utilizing the bulk/surface carrier-induced SOT effect, which was theoretically simulated using a four-band model in a sandwich configuration. Our work provides new insights into the fundamental properties of QAH insulators, for example, the interplay between magnetism and topology, which may help to usher in the next generation of quantum material-based computation and information technology.

#### Online content

Any methods, additional references, Nature Portfolio reporting summaries, source data, extended data, supplementary information, acknowledgements, peer review information; details of author contributions and competing interests; and statements of data and code availability are available at https://doi.org/10.1038/s41563-023-01694-y.

#### References

- Qi, X. L. & Zhang, S. C. Topological insulators and superconductors. Rev. Mod. Phys. 83, 1057–1110 (2011).
- Hasan, M. Z. & Kane, C. L. Colloquium: topological Insulators. Rev. Mod. Phys. 82, 3045–3067 (2010).
- Chang, C.-Z., Liu, C.-X. & MacDonald, A. H. Colloquium: quantum anomalous Hall effect. Rev. Mod. Phys. 95, 011002 (2023).
- 4. Haldane, F. D. M. Model for a quantum Hall effect without Landau levels: condensed-matter realization of the 'parity anomaly'. *Phys. Rev. Lett.* **61**, 2015–2018 (1988).
- Qi, X. L., Hughes, T. L. & Zhang, S. C. Topological field theory of time-reversal invariant insulators. *Phys. Rev. B* 78, 195424 (2008).
- Liu, C. X., Qi, X. L., Dai, X., Fang, Z. & Zhang, S. C. Quantum anomalous Hall effect in Hg<sub>1-y</sub>Mn<sub>y</sub>Te quantum wells. *Phys. Rev.* Lett. **101**, 146802 (2008).
- 7. Yu, R. et al. Quantized anomalous Hall effect in magnetic topological insulators. *Science* **329**, 61–64 (2010).
- Chang, C. Z. et al. Experimental observation of the quantum anomalous Hall effect in a magnetic topological insulator. Science 340, 167–170 (2013).
- Chang, C. Z. et al. High-precision realization of robust quantum anomalous Hall state in a hard ferromagnetic topological insulator. Nat. Mater. 14, 473–477 (2015).
- von Klitzing, K., Dorda, G. & Pepper, M. New method for high-accuracy determination of the fine-structure constant based on quantized Hall resistance. *Phys. Rev. Lett.* 45, 494–497 (1980).
- Kou, X. F. et al. Scale-invariant quantum anomalous Hall effect in magnetic topological insulators beyond the two-dimensional limit. Phys. Rev. Lett. 113, 137201 (2014).
- Checkelsky, J. G. et al. Trajectory of the anomalous Hall effect towards the quantized state in a ferromagnetic topological insulator. *Nat. Phys.* 10, 731–736 (2014).
- Ou, Y. et al. Enhancing the quantum anomalous Hall effect by magnetic codoping in a topological insulator. Adv. Mater. 30, 1703062 (2017).
- 14. Zhao, Y. F. et al. Tuning the Chern number in quantum anomalous Hall insulators. *Nature* **588**, 419–423 (2020).
- Mogi, M. et al. Magnetic modulation doping in topological insulators toward higher-temperature quantum anomalous Hall effect. Appl. Phys. Lett. 107, 182401 (2015).
- Tokura, Y., Yasuda, K. & Tsukazaki, A. Magnetic topological insulators. Nat. Rev. Phys. 1, 126–143 (2019).
- Manchon, A. et al. Current-induced spin-orbit torques in ferromagnetic and antiferromagnetic systems. Rev. Mod. Phys. 91, 035004 (2019).

- Fan, Y. B. et al. Electric-field control of spin-orbit torque in a magnetically doped topological insulator. *Nat. Nanotechnol.* 11, 352 (2016).
- Han, J. H. et al. Room-temperature spin-orbit torque switching induced by a topological Insulator. *Phys. Rev. Lett.* 119, 077702 (2017).
- Mogi, M. et al. Current-induced switching of proximity-induced ferromagnetic surface states in a topological insulator. *Nat. Commun.* 12, 1404 (2021).
- Wu, H. et al. Room-temperature spin-orbit torque from topological surface states. *Phys. Rev. Lett.* 123, 207205 (2019).
- Fan, Y. B. et al. Magnetization switching through giant spinorbit torque in a magnetically doped topological insulator heterostructure. *Nat. Mater.* 13, 699–704 (2014).
- Yasuda, K. et al. Current-nonlinear Hall effect and spin-orbit torque magnetization switching in a magnetic topological insulator. *Phys. Rev. Lett.* 119, 137204 (2017).
- Edelstein, V. M. Spin polarization of conduction electrons induced by electric current in two-dimensional asymmetric electron systems. Solid State Commun. 73, 233–235 (1990).
- Zhou, L.-J. et al. Confinement-induced chiral edge channel interaction in quantum anomalous Hall insulators. *Phys. Rev. Lett.* 130, 086201 (2023).
- Chang, C. Z. et al. Zero-field dissipationless chiral edge transport and the nature of dissipation in the quantum anomalous Hall state. *Phys. Rev. Lett.* 115, 057206 (2015).
- Wang, J., Lian, B. & Zhang, S. C. Universal scaling of the quantum anomalous Hall plateau transition. Phys. Rev. B 89, 085106 (2014).
- Lee, D. H., Wang, Z. Q. & Kivelson, S. Quantum percolation and plateau transitions in the quantum Hall effect. *Phys. Rev. Lett.* 70, 4130–4133 (1993).
- Jiang, J. et al. Concurrence of quantum anomalous Hall and topological Hall effects in magnetic topological insulator sandwich heterostructures. Nat. Mater. 19, 732–737 (2020).
- Garello, K. et al. Ultrafast magnetization switching by spin-orbit torques. Appl. Phys. Lett. 105, 212402 (2014).
- Liu, L. Q. et al. Spin-torque switching with the giant spin Hall effect of tantalum. Science 336, 555–558 (2012).

- 32. Liu, L. Q., Lee, O. J., Gudmundsen, T. J., Ralph, D. C. & Buhrman, R. A. Current-induced switching of perpendicularly magnetized magnetic layers using spin torque from the spin Hall effect. *Phys. Rev. Lett.* **109**, 096602 (2012).
- Chang, C. Z. et al. Observation of the quantum anomalous Hall insulator to Anderson insulator quantum phase transition and its scaling behavior. *Phys. Rev. Lett.* 117, 126802 (2016).
- 34. Fox, E. J. et al. Part-per-million quantization and current-induced breakdown of the quantum anomalous Hall effect. *Phys. Rev. B* **98**, 075145 (2018).
- 35. Lippertz, G. et al. Current-induced breakdown of the quantum anomalous Hall effect. *Phys. Rev. B* **106**, 045419 (2022).
- 36. Mellnik, A. R. et al. Spin-transfer torque generated by a topological insulator. *Nature* **511**, 449–451 (2014).
- Ghosh, S. & Manchon, A. Spin-orbit torque in a three-dimensional topological insulator-ferromagnet heterostructure: crossover between bulk and surface transport. *Phys. Rev. B* 97, 134402 (2018).
- Garate, I. & Franz, M. Inverse spin-galvanic effect in the interface between a topological insulator and a ferromagnet. *Phys. Rev.* Lett. 104, 146802 (2010).
- Ndiaye, P. B. et al. Dirac spin-orbit torques and charge pumping at the surface of topological insulators. *Phys. Rev. B* 96, 014408 (2017).
- 40. Liu, C. X. et al. Model Hamiltonian for topological insulators. *Phys. Rev. B* **82**, 045122 (2010).

**Publisher's note** Springer Nature remains neutral with regard to jurisdictional claims in published maps and institutional affiliations.

Springer Nature or its licensor (e.g. a society or other partner) holds exclusive rights to this article under a publishing agreement with the author(s) or other rightsholder(s); author self-archiving of the accepted manuscript version of this article is solely governed by the terms of such publishing agreement and applicable law.

© The Author(s), under exclusive licence to Springer Nature Limited 2023

#### Methods

#### MBE growth of QAH sandwich heterostructures

The 3-4-3 OAH sandwich heterostructures, specifically 3OL Cr-doped (Bi,Sb)<sub>2</sub>Te<sub>2</sub>/4QL (Bi,Sb)<sub>2</sub>Te<sub>2</sub>/3QL Cr-doped (Bi,Sb)<sub>2</sub>Te<sub>2</sub>, are fabricated using a commercial MBE system (Lab10, Omicron) with a base pressure lower than  $2 \times 10^{-10}$  mbar. In these QAH samples, the heavily Cr-doped  $(Bi,Sb)_2Te_3$  layer [that is, x = 0.24 in  $(Bi,Sb)_{2-x}Cr_xTe_3$ ] is in a trivial insulator regime, so the two non-trivial surface states are formed at the interfaces between the middle undoped TI layers and the surface magnetic TI layers 14,41. Before the growth of the QAH samples, the heat-treated insulating SrTiO<sub>3</sub>(111) substrates are first outgassed at 600 °C for 1 h. Next, high-purity Bi (99.9999%), Sb (99.9999%), Cr (99.999%) and Te (99.9999%) are evaporated from Knudsen effusion cells. During the growth of the OAH sandwich samples, the substrate is maintained at ~230 °C and the Bi/Sb ratio is fixed at ~0.5 for all three layers. The flux ratio of Te per (Bi + Sb + Cr) is set to greater than ~10 to prevent Te deficiency in the films. The growth rate for the QAH sandwiches is ~0.2 QL per minute. To avoid possible contamination and degradation under ambient conditions, a ~3-nm-thick layer of Al<sub>2</sub>O<sub>3</sub> is deposited on top of the QAH sandwich heterostructures using an atomic layer deposition system as soon as they were removed from the MBE chamber.

#### Electron-beam lithography of the QAH Hall bar devices

The QAH sandwich heterostructures with a -3-nm-thick  $Al_2O_3$  capping layer are patterned into Hall bar devices with a width w of -1–10  $\mu$ m using two-step electron-beam lithography. For all of the Hall bar devices used in this work, the aspect ratio is -4. We use Cr (10 nm)/Au (30 nm) layers as the electrodes of these Hall bar devices. Before deposition of the Cr/Au electrodes using electron-beam evaporation, the -3-nm-thick  $Al_2O_3$  layer is etched using CD26 alkaline developer. Finally, we use Ar plasma to etch the QAH sandwich into the Hall bar geometry. To avoid the charging effect, we deposit a -20-nm-thick layer of Au on top of the resist before electron-beam lithography.

#### **Electrical-transport measurements**

Transport measurements are carried out using both a PPMS (Quantum Design; DynaCool, 1.7 K, 9 T) and a dilution refrigerator cryostat (Bluefors; 10 mK) with a vector magnet (Bluefors; 9-1-1 T). The bottom gate voltage  $V_{\rm g}$  is applied using a Keithley 2450 meter. The excitation currents used in the PPMS ( $\geq$ 1.7 K) and dilution (-20 mK) measurements are 10 nA and 1 nA, respectively. The results reported here have been reproduced in around ten Hall bar devices with a width from 1 to 10  $\mu m$  using our PPMS and around five Hall bar devices with a width from 1 to 5  $\mu m$  using our dilution refrigerator (Extended Data Figs. 5 and 10). The current pulse with a duration of 5 ms, parallel to the in-plane magnetic field, is applied using a Keithley 6221 source meter. The current pulse density  $J_{\rm pulse}$  used for magnetization switching is similar in all devices of different widths. More transport results are shown in Extended Data Figs. 1–10 and Supplementary Information.

### Numerical simulations on SOT in QAH sandwich heterostructures

To numerically solve the spectrum of the four-band Hamiltonian, we use the basis

$$\psi(z) = \langle z | k_{\parallel} N \lambda \rangle = \sqrt{2/L} \sin N \pi z / L | k_{\parallel} \lambda \rangle,$$

where  $\lambda$  is the orbital and spin degrees of freedom;  $\sqrt{2/L} \sin N\pi z/L$  with N as a positive integer satisfies the open boundary condition  $\psi(z=0)=\psi(z=L)=0$  in the z direction of a thin film. For L=10 nm in our QAH sandwiches, N is truncated at  $N_{\rm max}=30$ , which is large enough to reproduce the gapless Dirac surface states for M=0 eV.

From the Hamiltonian, the response function of spin polarization can be obtained from the Kubo formula  $^{42}$ 

$$\begin{split} \chi_{yx} &= e\hbar \sum_{n} \int \frac{\mathrm{d}^{2}k_{\parallel}}{\left(2\pi\right)^{2}} \chi_{yx}\left(k_{\parallel}, n, E_{F}\right) \\ &= -\frac{e\hbar}{4\pi} \sum_{n} \int \frac{\mathrm{d}^{2}k_{\parallel}}{\left(2\pi\right)^{2}} \frac{2\Gamma^{2}}{\left(\left(E_{F} - E_{k_{\parallel}n}\right)^{2} + \Gamma^{2}\right)^{2}} \langle k_{\parallel}n | \sigma_{y} | k_{\parallel}n \rangle \langle k_{\parallel}n | \nu_{x} | k_{\parallel}n \rangle. \end{split}$$

Here,  $E_{k_\parallel n}$  and  $|k_\parallel n\rangle$  are the nth energies and eigenstates of Hamiltonian, respectively.  $v_x$  is  $\partial_{kx}H$  is the velocity operator. The contribution on the Fermi surfaces is defined as  $\chi_{yx}\left(k_xn,E_F=E_{k_\parallel n}\right)$  with  $k_\parallel=k_x\hat{x}$  taken as the typical point on the Fermi surfaces. The parameter  $\Gamma$  is the self-energy broadening from disorder, where  $\Gamma=0.03$  eV is used. In Supplementary Section 13, we also perform the numerical simulations on the Landau–Lifshitz–Gilbert equation to show the effects of  $\tau_{\text{SO,ISGE}}$  in the magnetization switch.

To further understand  $\chi_{yx}$ , the two-surface-state model is used with the Hamiltonian

$$H_{2s} = \begin{pmatrix} -v_{\rm F}(k_y\sigma_x-k_x\sigma_y) + M\sigma_z + V_0/2 & 0 \\ 0 & v_{\rm F}(k_y\sigma_x-k_x\sigma_y) + M\sigma_z - V_0/2 \end{pmatrix}.$$

The first (second) diagonal block is the top (bottom) surface;  $v_F$  is the Fermi velocity, M is the magnetization and  $V_0$  is the asymmetric potential between two surfaces. In Fig. 5a, M = 0.041 eV and  $V_0$  = 0.032 eV are fitted from the surface-state spectrum of  $E_F$  > -0.15 eV.

#### **Data availability**

The datasets generated during and/or analysed during this study are available from the corresponding author upon reasonable request.

#### References

- 41. Zhao, Y.-F. et al. Zero magnetic field plateau phase transition in higher Chern number quantum anomalous Hall insulators. *Phys. Rev. Lett.* **128**, 216801 (2022).
- 42. Mahan, G. D. Many-Particle Physics 2nd edn (Springer, 1990).

#### **Acknowledgements**

We thank Y.-T. Cui, Y.-B. Fan, I. Garate, L.-Q. Liu, A. H. MacDonald, N. Samarth, J. Shi, W.-D. Wu, D. Xiao and X.-D. Xu for helpful discussions. This work is primarily supported by an ARO Award (W911NF2210159) (C.-Z.C.), including sample synthesis and device fabrication. The PPMS measurements are supported by an AFOSR grant (FA9550-21-1-0177) (C.-Z.C.) and an NSF-CAREER award (DMR-1847811) (C.-Z.C.). The theoretical calculations and simulations are supported by the Penn State MRSEC for Nanoscale Science (DMR-2011839) (C.-X.L. and C.-Z.C.) and an NSF grant (DMR-2241327) (C.-X.L. and C.-Z.C.). C.-Z.C. acknowledges the support from the Gordon and Betty Moore Foundation EPiQS Initiative (GBMF9063 to C.-Z.C.).

#### **Author contributions**

C.-Z.C. conceived and designed the experiment. Y.-F.Z. and D.Z. grew the QAH sandwich samples. L.-J.Z. fabricated the Hall bar devices using electron-beam lithography. W.Y., L.-J.Z., R.Z., Z.Y., Y.W., H.Y., M.H.W.C. and M.K. performed the electrical-transport measurements. K.Y., R.M. and C.-X.L. carried out the numerical simulations and provided theoretical support. W.Y., K.Y., C.-X.L. and C.-Z.C. analysed the data and wrote the manuscript with inputs from all authors.

#### **Competing interests**

The authors declare no competing interests.

#### **Additional information**

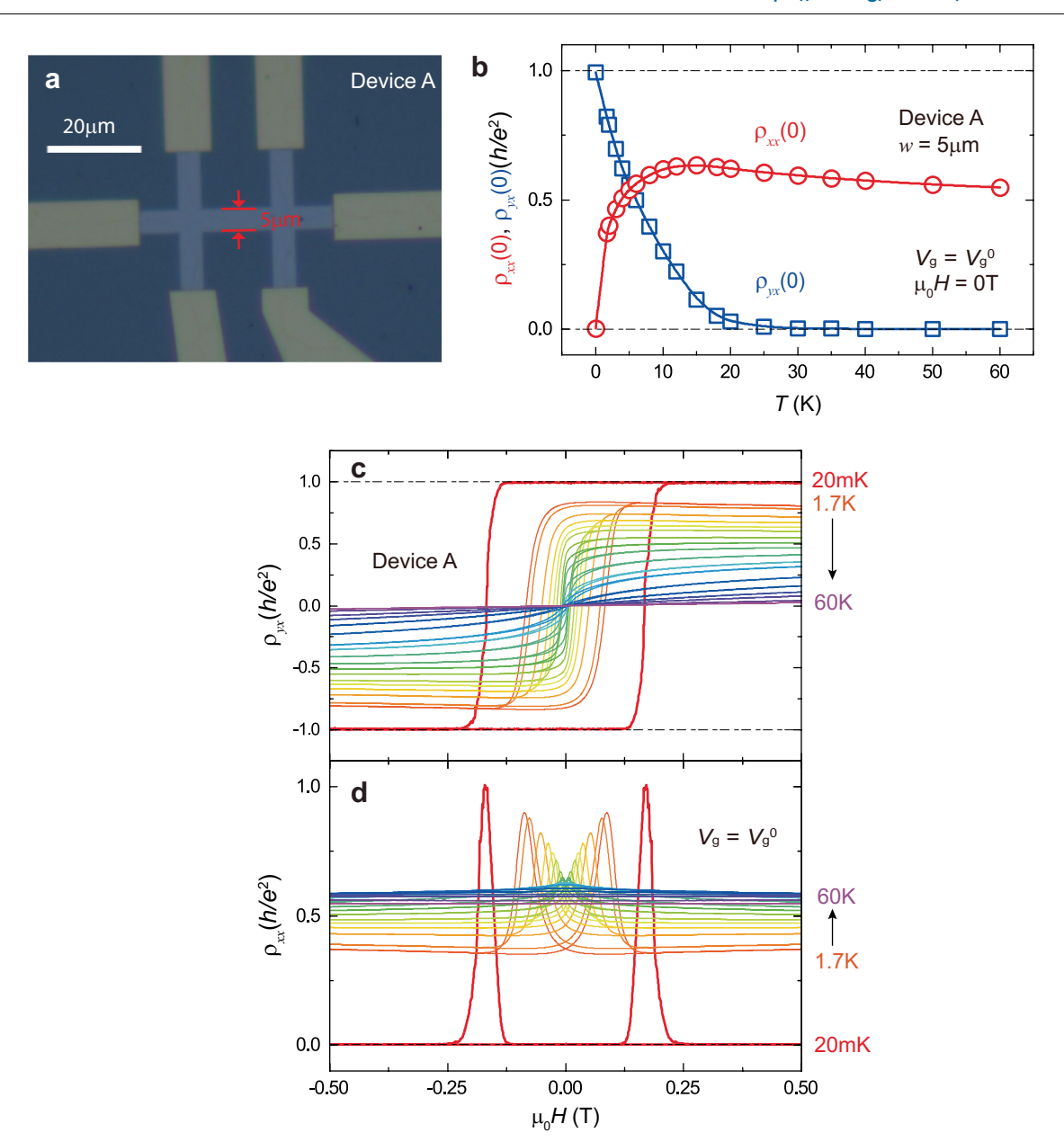
**Extended data** is available for this paper at https://doi.org/10.1038/s41563-023-01694-y.

**Supplementary information** The online version contains supplementary material available at https://doi.org/10.1038/s41563-023-01694-y.

**Correspondence and requests for materials** should be addressed to Chao-Xing Liu or Cui-Zu Chang.

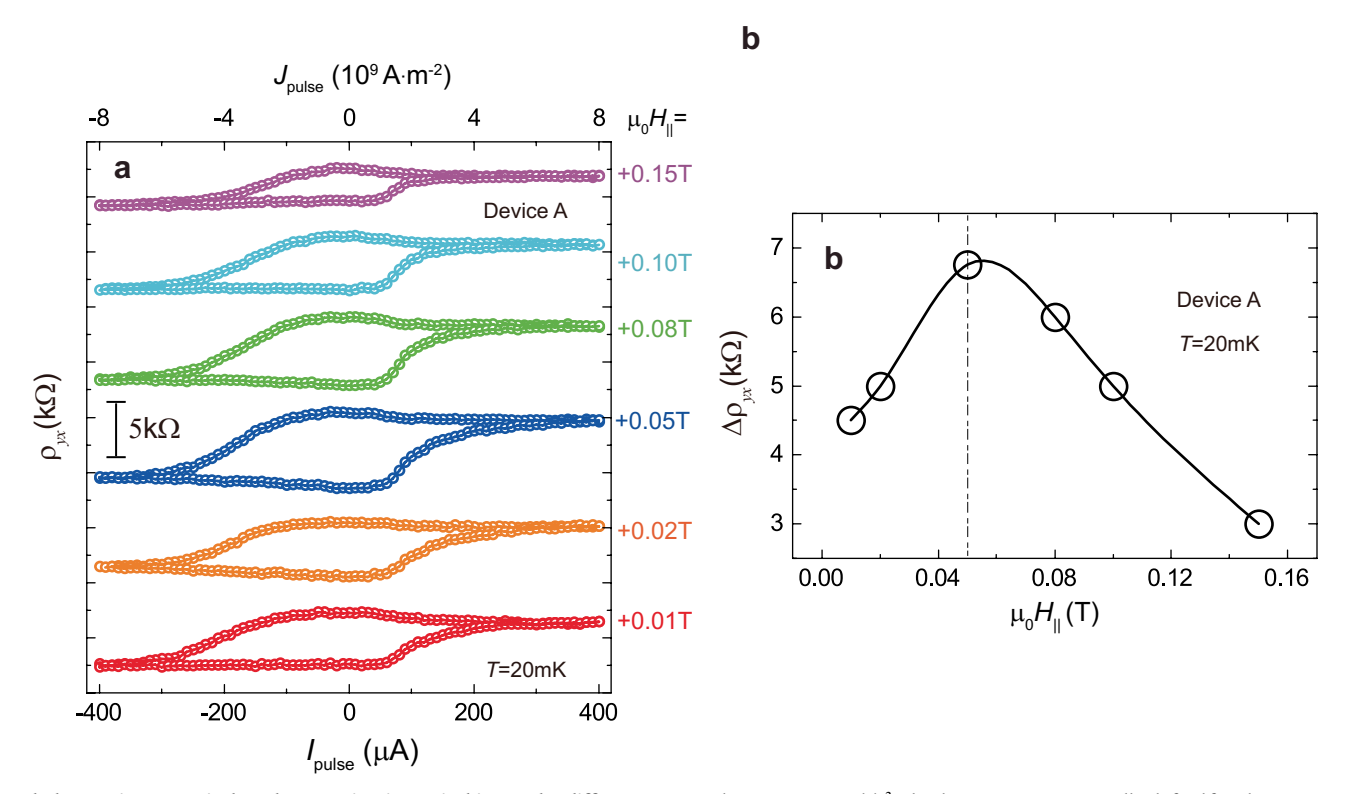
**Peer review information** *Nature Materials* thanks Philip Moll and the other, anonymous, reviewer(s) for their contribution to the peer review of this work.

**Reprints and permissions information** is available at www.nature.com/reprints.



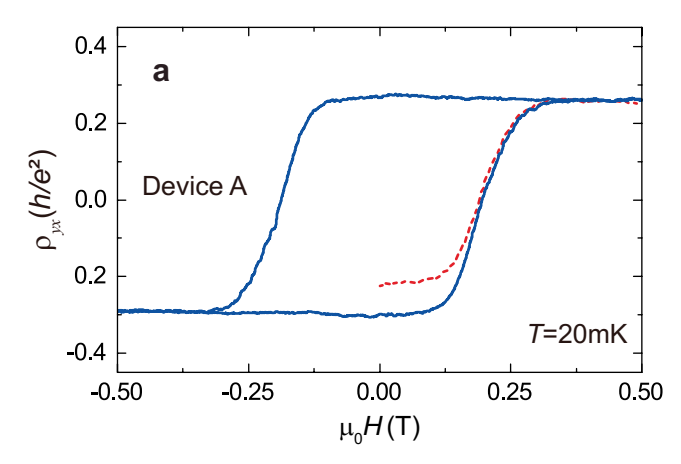
**Extended Data Fig. 1** | **QAH state in Device A** ( $w = 5 \mu m$ ). **a**, The optical photograph of Device A. The effective area of the Hall bar device is 20  $\mu m \times 5 \mu m$ . **b**, Temperature dependence of  $\rho_{yx}(0)$  (blue squares) and  $\rho_{xx}(0)$  (red circles) at

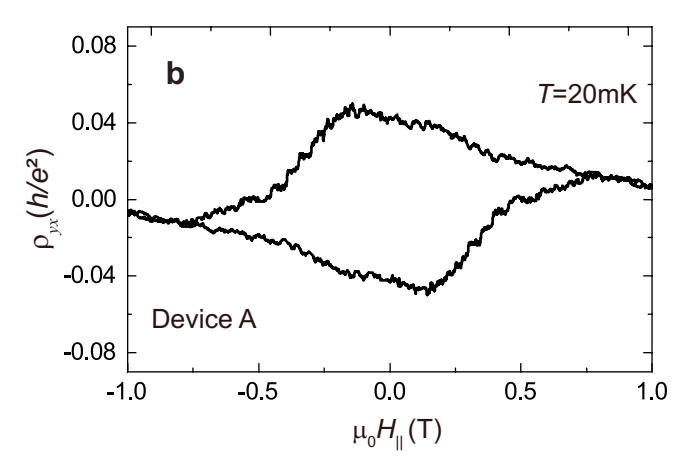
 $V_{\rm g} = V_{\rm g}^{~0}$ . All measurements are taken at  $\mu_0 H = 0$  T after magnetic field training. The critical temperature of the QAH state in Device A is -5.3 K. **c**, **d**,  $\mu_0 H$  dependence of  $\rho_{\rm yx}$  and  $\rho_{\rm xx}$  measured at different temperatures and  $V_{\rm g} = V_{\rm g}^{~0}$ .



Extended Data Fig. 2 | SOT-induced magnetization switching under different in-plane magnetic fields in Device A. a, Current pulse  $I_{\rm pulse}$  dependence of  $\rho_{yx}$  under different  $\mu_0 H_{\parallel}$  at T = 20 mK. The corresponding current pulse density  $J_{\rm pulse}$  is shown on the upper horizontal axis. The hysteresis loops reflect the reversal of magnetization direction. All these SOT switching measurements

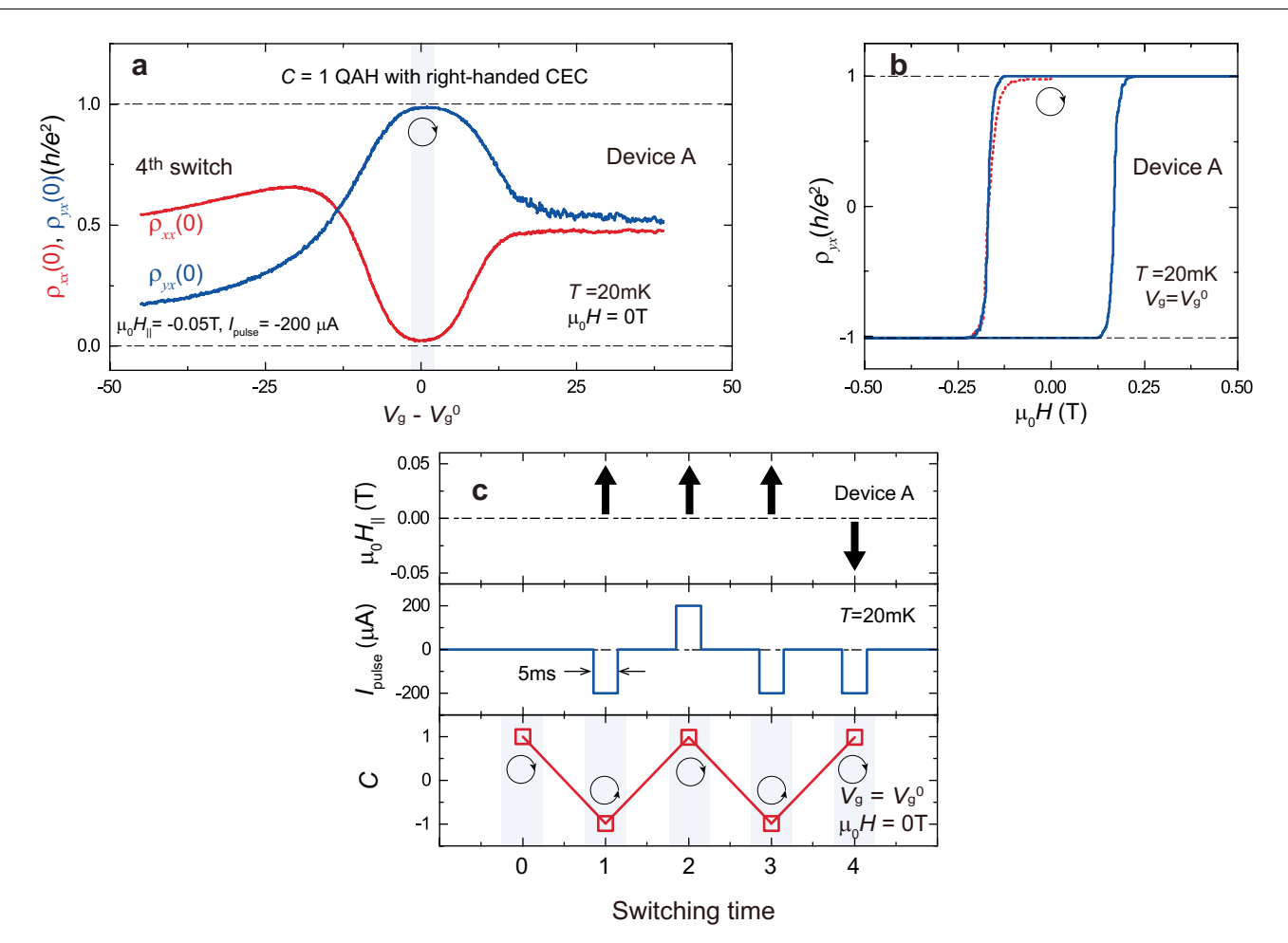
are done at  $\rho_{yx}$  - 0.27  $h/e^2$ . The data curves are vertically shifted for clarity. **b**,  $\mu_0 H_{||}$  dependence of the Hall resistance change  $\Delta \rho_{yx}$  at T=20 mK.  $\Delta \rho_{yx}$  is maximized near  $\mu_0 H_{||}=+0.05$  T, so we choose  $|\mu_0 H_{||}|=0.05$  T for the SOT-induced magnetization switching in Device A.





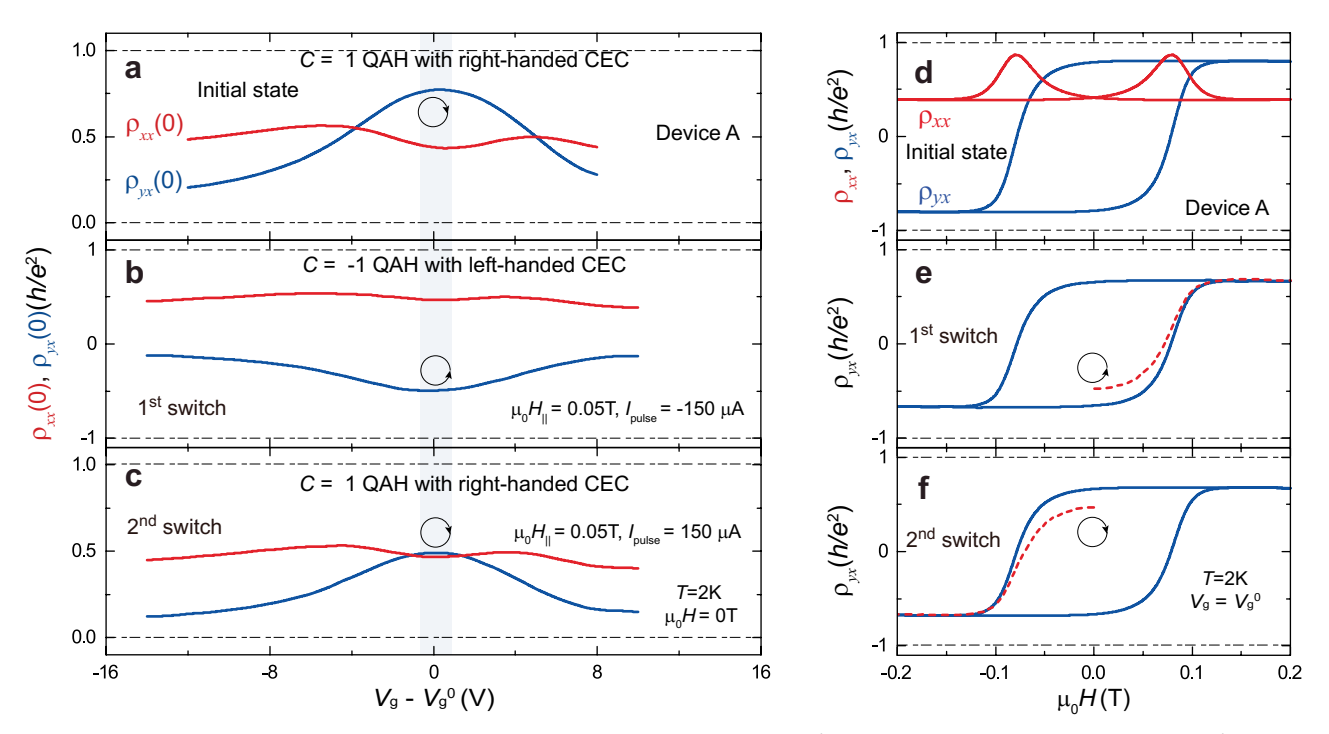
**Extended Data Fig. 3** | **More magneto-transport properties of Device A. a**,  $\mu_0 H$  dependence of  $\rho_{yx}$  without tuning  $V_{\rm g}$  after SOT switching at  $\rho_{yx}(0)$  - 0.27  $h/e^2$  and T=20 mK. After SOT-induced switching,  $\rho_{yx}(0)$  is  $\sim$  -0.225  $h/e^2$ . After applying  $\mu_0 H \sim 0.5$  T to align the magnetization,  $\rho_{yx}(0) \sim 0.268 \, h/e^2$ . Therefore, the SOT magnetization switching ratio at  $\rho_{yx}(0) \sim 0.27 \, h/e^2$  by applying  $|I_{\rm pulse}|$ -200  $\mu$ A under  $\mu_0 H_{\parallel} = +0.05$  T is  $\sim 0.225/0.268 = 83.9\%$ . Here the switching ratio is defined as the absolute value of the zero magnetic field Hall resistance ratio before and

after magnetic training. When the sample magnetization is fully aligned, the negligible  $\rho_{yx}$  difference suggests the gating effect induced by the injection of  $I_{pulse}$  is much weaker when the SOT switching is done at  $|\rho_{yx}(0)| - 0.27 \ h/e^2$ . The red dashed curve corresponds to the initial magnetization process after SOT switching. **b**,  $\mu_0 H_{\parallel}$  dependence of  $\rho_{yx}$  at T=20 mK when the sample is tuned to  $\rho_{yx}(0) - 0.27 \ h/e^2$ . We find that the anisotropy field K is -0.7 T and thus the sample magnetization almost points upward and downward under  $|\mu_0 H_{\parallel}| = 0.05$  T.



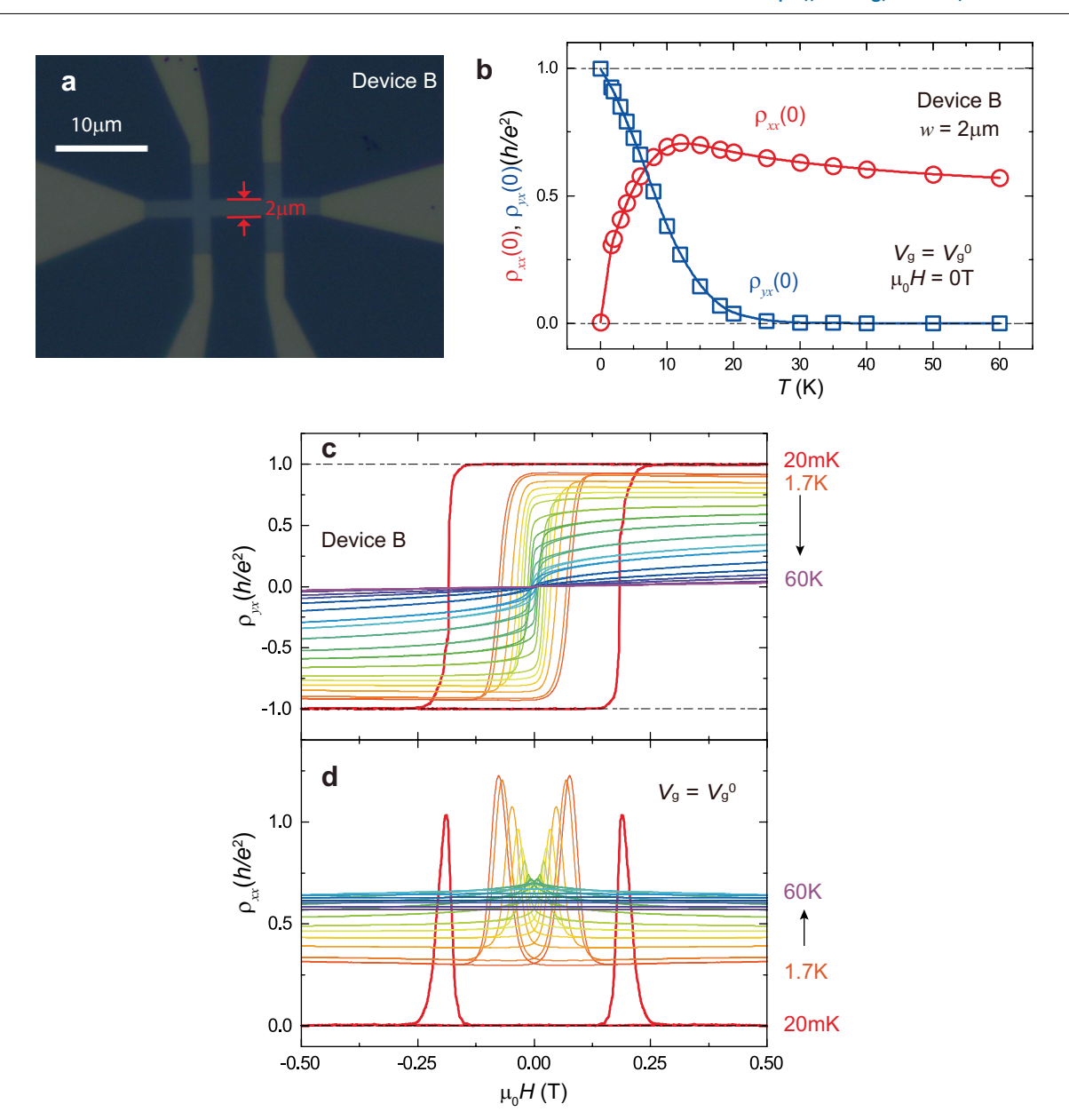
Extended Data Fig. 4 | Electrical switching of edge current chirality in Device A through bulk and surface carriers generated SOT. a, Gate  $(V_{\rm g} - V_{\rm g}^{\, 0})$  dependence of  $\rho_{\rm yx}(0)$  (blue) and  $\rho_{\rm xx}(0)$  (red) of the QAH insulator after the fourth switch with  $I_{\rm pulse}$  ~  $-200~\mu{\rm A}$  under  $\mu_0 H_{\rm H} = -0.05~{\rm T}$ . The SOT switching is done at  $\rho_{\rm yx}(0)$  ~  $-0.27~h/e^2$  and  $T = 20~{\rm mK}$ . b,  $\mu_0 H$  dependence of  $\rho_{\rm yx}$  at  $V_{\rm g} = V_{\rm g}^{\, 0}$  and  $T = 20~{\rm mK}$  after the fourth switch. The red dashed curve corresponds to the initial

magnetization process after the SOT switching.  $\mathbf{c}$ , Summary of all four switches of CEC chirality at T=20 mK. The CEC chirality can be switched by changing the direction of either the in-plane magnetic field or the current pulse. Note that the SOT switching is independent of the initial direction of magnetization M (Supplementary Figs. 11 and 12). Therefore, the reversed magnetization should be independent of the number of switching times.



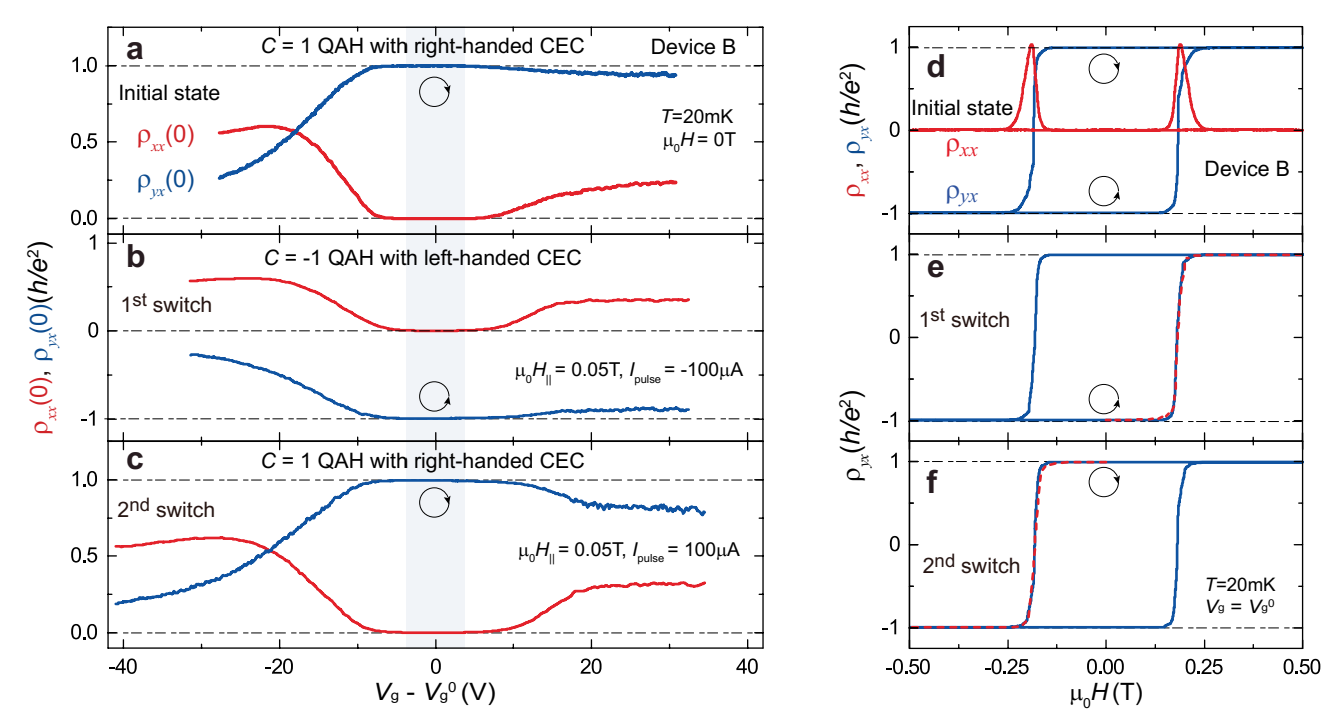
Extended Data Table. 5 | Electrical switching of edge current chirality in Device A at T=2 K. a-c, Gate  $(V_{\rm g}-V_{\rm g}^{\,0})$  dependence of  $\rho_{\rm px}(0)$  (blue) and  $\rho_{\rm xx}(0)$  (red) of the QAH insulator with right-handed CEC (that is the initial state) (a), after the first (b) and second (c) switches. d,  $\mu_0 H$  dependence of  $\rho_{\rm px}$  (blue) and

 $\rho_{xx}$  (red) at  $V_g = V_g^{\ 0}$  and T = 2 K. **e, f**,  $\mu_0 H$  dependence of  $\rho_{yx}$  at  $V_g = V_g^{\ 0}$  and T = 2 K after the first (**e**) and second (**f**) switches, respectively. The red dashed curves correspond to the initial magnetization process after each switch.



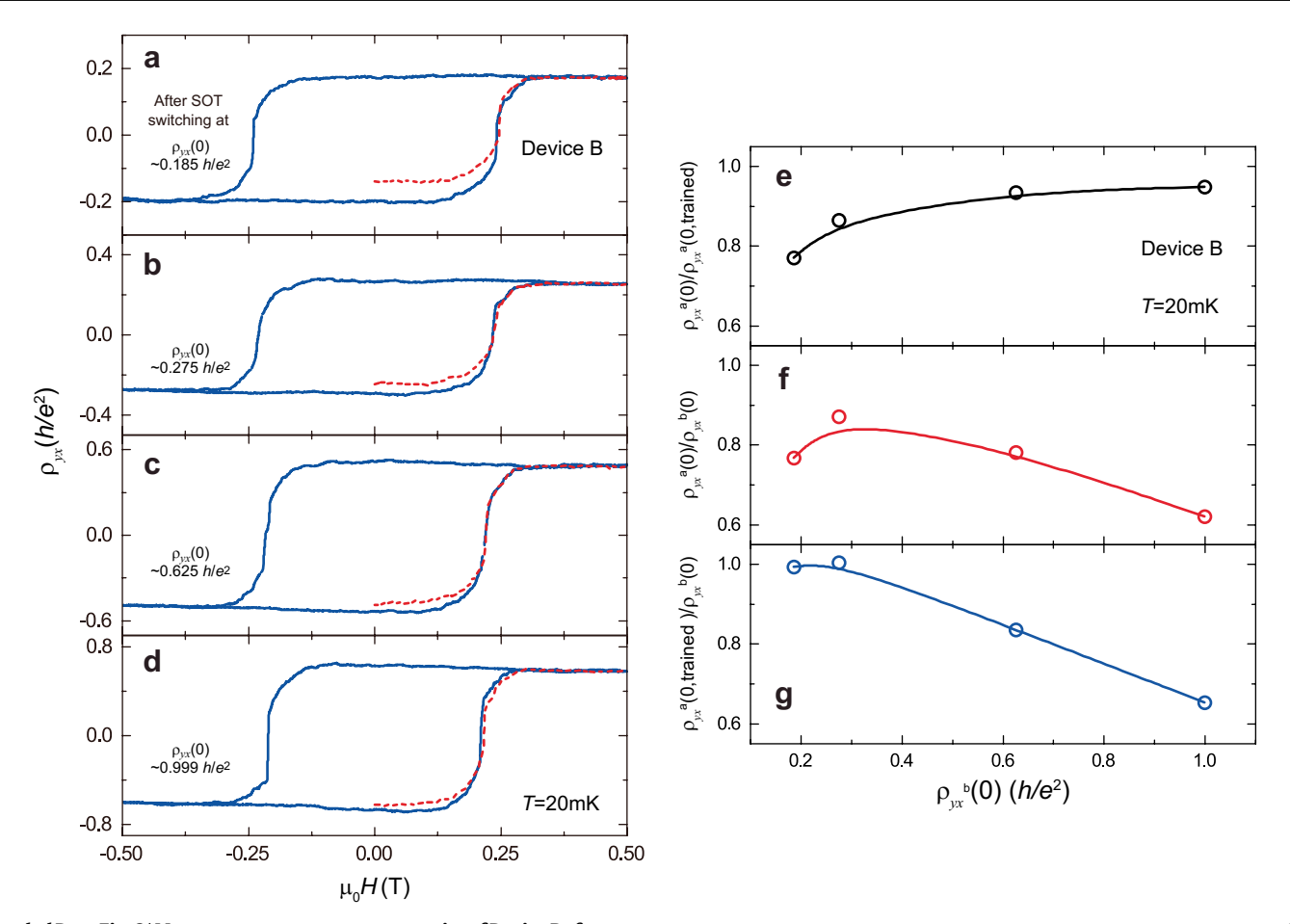
**Extended Data Fig. 6** | **QAH state in Device B (w = 2 \mum).** a, The optical photograph of Device B. The effective area of the Hall bar device is 8  $\mu$ m × 2  $\mu$ m. b, Temperature dependence of  $\rho_{yx}(0)$  (blue squares) and  $\rho_{xx}(0)$  (red circles) at

 $V_{\rm g} = V_{\rm g}^{~0}$ . All measurements are taken at  $\mu_0 H = 0$  T after magnetic field training. The critical temperature of the QAH state in Device B is -6.8 K. c, d,  $\mu_0 H$  dependence of  $\rho_{\rm yx}$  and  $\rho_{\rm xx}$  measured at different temperatures and  $V_{\rm g} = V_{\rm g}^{~0}$ .



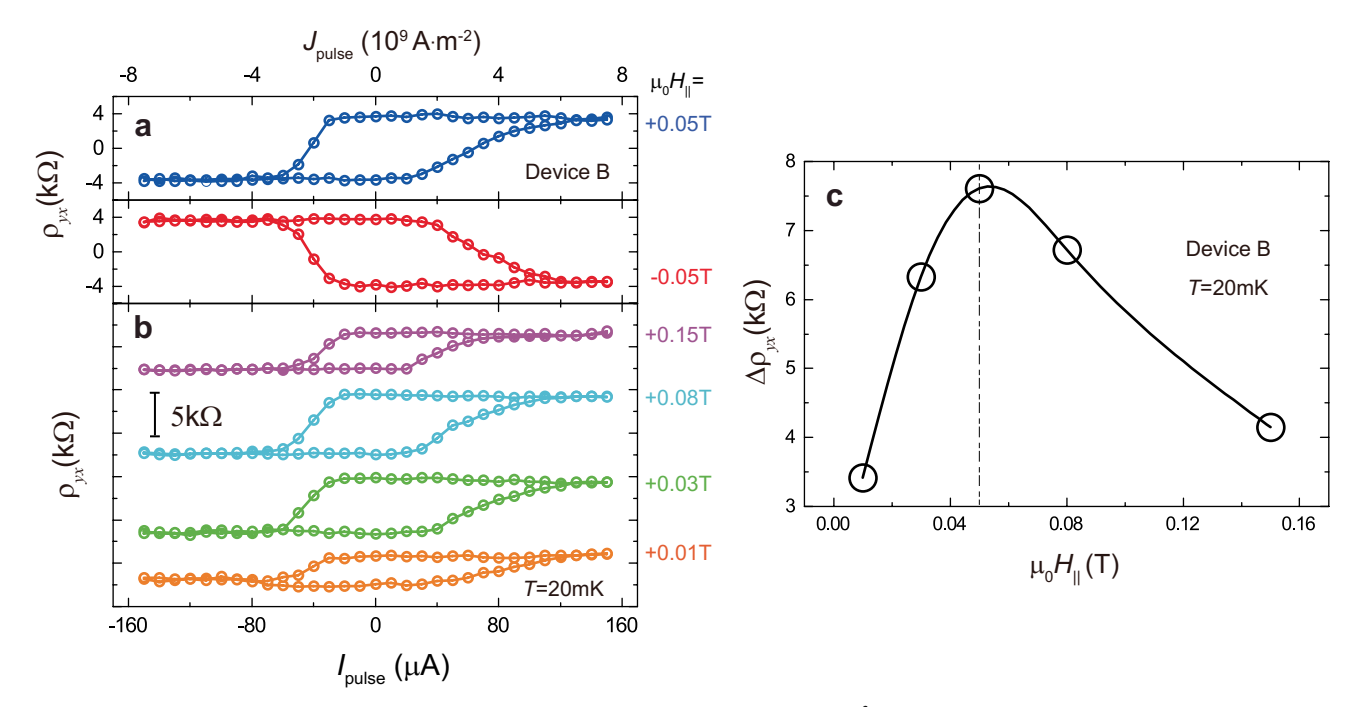
Extended Data Fig. 7 | Electrical switching of edge current chirality in Device B through bulk and surface carriers generated SOT. a-c, Gate  $(V_{\rm g}-V_{\rm g}^0)$  dependence of  $\rho_{yx}(0)$  (blue) and  $\rho_{xx}(0)$  (red) of the QAH insulator with the right-handed CEC (that is the initial state) (a), after the first switch with  $I_{\rm pulse}$  ~ -100  $\mu$ A (b) and the second switch with  $I_{\rm pulse}$  ~ 100  $\mu$ A (c) under  $\mu_0 H_{\parallel}$  ~ +0.05 T. Both SOT switches are done at  $|\rho_{yx}(0)|$  ~ 0.27  $h/e^2$  and T = 20 mK. d,  $\mu_0 H$  dependence

of  $\rho_{yx}$  (blue) and  $\rho_{xx}$  (red) at  $V_g = V_g^0$  and T = 20 mK. **e**, **f**,  $\mu_0 H$  dependence of  $\rho_{yx}$  at  $V_g = V_g^0$  and T = 20 mK after the first (**e**) and second (**f**) switches. The red dashed curves correspond to the initial magnetization process after each switch.  $V_g^0$ s are +1.0 V, +22.5 V, and +35.5 V for the initial state, after  $1^{\rm st}$  switch, and after  $2^{\rm nd}$  switch, respectively.



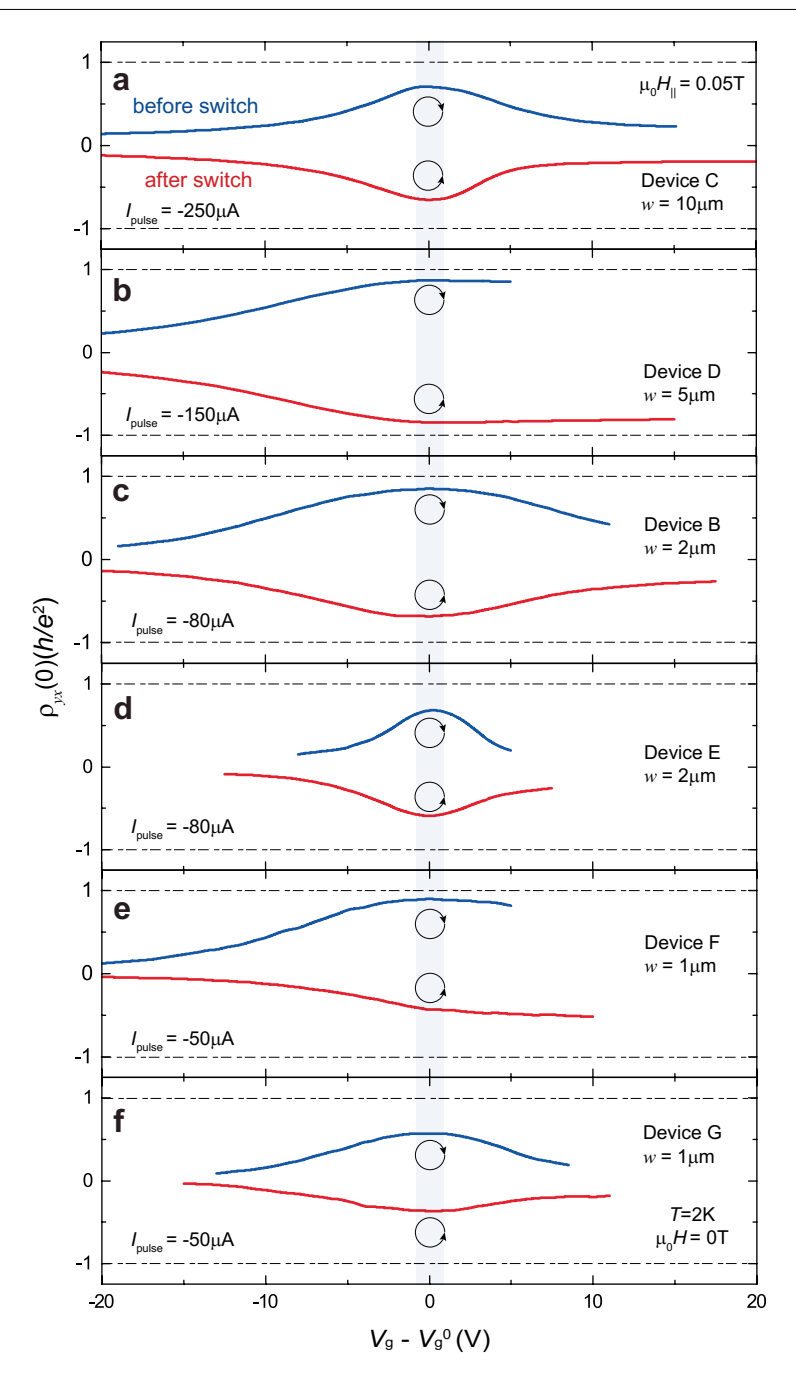
**Extended Data Fig. 8** | **More magneto-transport properties of Device B after SOT switching. a-d**,  $\mu_0 H$  dependence of  $\rho_{yx}$  without tuning  $V_g$  after SOT switching at  $\rho_{yx}(0) - 0.185 \, h/e^2(\mathbf{a})$ ,  $-0.275 \, h/e^2(\mathbf{b})$ ,  $-0.625 \, h/e^2(\mathbf{c})$ , and  $-0.999 \pm 0.001 \, h/e^2(\mathbf{d})$ , respectively. After SOT-induced switching, the corresponding  $\rho_{yx}(0)$  is  $-0.142 \, h/e^2(\mathbf{a})$ ,  $-0.240 \, h/e^2(\mathbf{b})$ ,  $-0.489 \, h/e^2(\mathbf{c})$ , and  $-0.620 \, h/e^2(\mathbf{d})$ , respectively. After applying  $\mu_0 H$  - 0.5 T to align the magnetization,  $\rho_{yx}(0)$  becomes  $-0.184 \, h/e^2(\mathbf{a})$ ,  $-0.277 \, h/e^2(\mathbf{b})$ ,  $-0.523 \, h/e^2(\mathbf{c})$ , and  $-0.653 \, h/e^2(\mathbf{d})$ , respectively. The red dashed curve corresponds to the initial magnetization

process after each switch. **e-g**, Three ratios  $\rho_{yx}^{a}(0)/\rho_{yx}^{a}(0)$ , trained) (**e**),  $\rho_{yx}^{a}(0)/\rho_{yx}^{b}(0)$  (**f**),  $\rho_{yx}^{a}(0)$ , trained)/ $\rho_{yx}^{b}(0)$  (**g**) as a function of  $\rho_{yx}^{b}(0)$ , where the SOT switching is done.  $\rho_{yx}^{b}(0)$ : the zero magnetic field Hall resistance before SOT switching.  $\rho_{yx}^{a}(0)$ : the zero magnetic field Hall resistance after SOT switching.  $\rho_{yx}^{a}(0)$ : trained): the zero magnetic field Hall resistance after SOT switching and  $\mu_{0}H - 0.5$  T training. All measurements are taken at T = 20 mK. For the SOT switching done near the QAH regime, the  $\rho_{yx}^{a}(0)/\rho_{yx}^{b}(0)$  ratio cannot be used to estimate the magnetization switching ratio since  $\rho_{yx} \sim M$  becomes invalid.



Extended Data Fig. 9 | SOT-induced magnetization switching under different in-plane magnetic fields in Device B ( $w=2~\mu m$ ). a, Current pulse  $I_{\rm pulse}$  dependence of  $\rho_{yx}$  under  $\mu_0 H_{\parallel}$  = +0.05 T (top) and  $\mu_0 H_{\parallel}$  = -0.05 T (bottom) at  $T=20~{\rm mK}$ . b,  $I_{\rm pulse}$  dependence of  $\rho_{yx}$  under different  $\mu_0 H_{\parallel}$  at  $T=20~{\rm mK}$ . The corresponding current pulse density  $J_{\rm pulse}$  in (a) and (b) is shown on the upper horizontal axis. All these SOT switching measurements in (a) and (b) are

done at  $\rho_{yx}$  - 0.27  $h/e^2$ . The data curves in (b) are vertically shifted for clarity. c,  $\mu_0 H_{\parallel}$  dependence of the Hall resistance change  $\Delta \rho_{yx}$  at T=20 mK.  $\Delta \rho_{yx}$  is maximized near  $\mu_0 H_{\parallel}=+0.05$  T, so we chose  $|\mu_0 H_{\parallel}|=0.05$  T for the SOT-induced magnetization switching in Device B. We find that the optimal  $\mu_0 H_{\parallel}$  for the SOT-induced magnetization switching is independent of the width of the QAH Hall bar device.



Extended Data Fig. 10 | Electrical switching of edge current chirality in more QAH insulator devices at T=2 K. a-f, Gate  $(V_g-V_g^0)$  dependence of  $\rho_{yx}(0)$  before (blue) and after (red) SOT magnetization switching in Device C  $(w=10~\mu m)$  (a), Device D  $(w=5~\mu m)$  (b), Device B  $(w=2~\mu m)$  (c), Device E

 $(w=2~\mu m)$  (**d**), Device F  $(w=1~\mu m)$  (**e**), and Device G  $(w=1~\mu m)$  (**f**), respectively. The SOT-induced magnetization switching is all done at  $\rho_{yx}(0)$  - 0.155  $h/e^2$  and T=2~K under  $\mu_0 H_{\parallel} \sim +0.05~T$ . The current pulse  $I_{pulse}$  used for SOT magnetization switching becomes smaller by reducing the width of the QAH Hall bar device.